Regional circulation of the Monterey Bay region: Hydrostatic versus nonhydrostatic modeling

Yu-Heng Tseng[1]
Environmental Fluid Mechanics Laboratory, Stanford University, Stanford, California, USA

David E. Dietrich
AcuSea Inc., Albuquerque, New Mexico, USA

Joel H. Ferziger
Environmental Fluid Mechanics Laboratory, Stanford University, Stanford, California, USA

Received 1 October 2003; revised 6 March 2005; accepted 6 May 2005; published 23 September 2005.

[1] Ocean circulation off the west coast of the United States is driven by a variety of mechanisms, the most important of which are the seasonally varying local wind stress and coastal irregularities. Remote forcing is also important and expressed through the open boundary conditions. We use a nonhydrostatic, Dietrich/Center for Air-Sea Technology (DieCAST) ocean model to simulate the regional circulation in the vicinity of Monterey Bay, California. Satellite images often show a cyclonic eddy in the bay and an anticyclonic eddy outside the bay during spring and summer. We compare the simulation results with observed mooring and HF radar-derived velocity data. The coastal geometry plays an important role in the generation and movement of coastal eddies. Quantitative comparisons between hydrostatic and nonhydrostatic models are made to investigate the importance of the nonhydrostatic effects in coastal ocean simulation. The results show that both the Sur Ridge area and the Monterey Submarine Canyon contribute significantly to nonhydrostatic effects and small-scale features. The strong nonhydrostatic and small-scale features result from the California Undercurrent flows across sloping bathymetry and interactions with near-surface California Current in summer. Rapid changes in slope in the presence of strong flows cause vertical acceleration, which violates the hydrostatic approximation. Surface-trapped nonhydrostatic fronts also occur frequently in the shallow ocean during winter. These effects have seasonal variation and cannot be ignored in coastal ocean modeling with complex bathymetry.

Citation: Tseng, Y.-H., D. E. Dietrich, and J. H. Ferziger (2005), Regional circulation of the Monterey Bay region: Hydrostatic versus nonhydrostatic modeling, *J. Geophys. Res.*, *110*, C09015, doi:10.1029/2003JC002153.

1. Introduction

[2] Monterey Bay is located 100 km south of San Francisco and is one of several large bays on the West Coast of the United States. This area is important because of the abundance of marine life, and many studies have examined the circulation in its vicinity [*Rosenfeld et al.*, 1994; *Ramp et al.*, 1997; *Collins et al.*, 2000]. They found that the circulation is highly correlated to the California Current System (CCS). Generally speaking, the CCS is composed of two parts (Figure 1). In the offshore region, flow is dominated by a broad, weak (10–30 cm/s), shallow (0–500 m) equatorward flowing current, the California Current (CC). The CC extends offshore to a distance of 900–1000 km and flows year-round [*Lynn and Simpson*, 1987]. Within about 100 km of the coast, two narrow poleward flowing boundary currents have been found, the Inshore Countercurrent (IC) and the California Undercurrent (CUC). They are distinguished by the properties of the water they transport. Three different water masses are found in CCS [*Lynn and Simpson*, 1987]; the Pacific Subarctic (upper 200 m), the North Pacific Central and the Equatorial Pacific (subsurface). The IC is a weak current that varies seasonally, appearing in fall and winter, and transports shallow, upper layer water. It has different names depending on location, e.g., the Davidson Current (north of Point Conception), and the Southern California Countercurrent (south of Point Conception). The CUC is a narrow (10–50 km) relatively weak subsurface flow and transports warm, saline equatorial water [*Batteen and Vance*, 1998]. *Hickey* [1979] found that the core flow of CUC occurs at roughly 200 m depth. In a recent triennial National Marine Fisheries Service (NMFS) survey of Pacific whiting, *Pierce et al.* [2000] found a poleward CUC core (velocity greater than 10 cm/s) with thickness 200–300 m, 20–25 km off the shelf break.

[1]Now at Computational Research Division, Lawrence Berkeley National Laboratory, Berkeley, California, USA.

0148-0227/05/2003JC002153$09.00

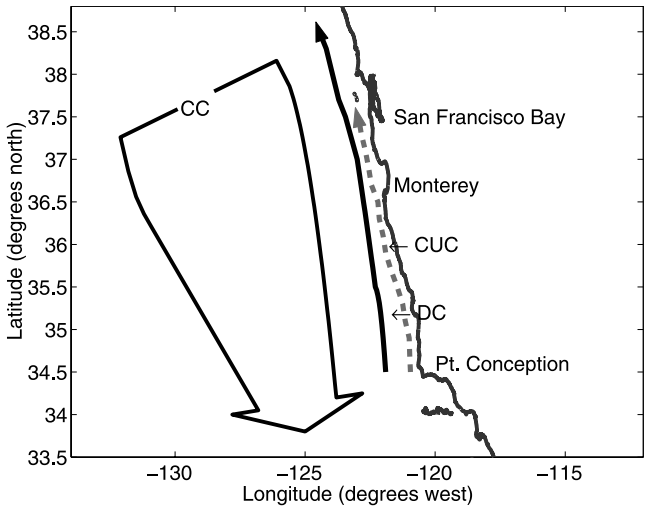

Figure 1. Schematic diagram of the California Current System (CCS). CC, California Current; CUC, California Undercurrent; DC, Davidson Current (only appearing in fall and winter). See color version of this figure in the HTML.

In general, the CUC is strongest at around 200–300 m depth and has a mean speed of approximately 15 cm/s [*Pierce et al.*, 2000] at all latitudes on the west coast throughout the year. These are mean climatological annual cycle features; there are also some significant interannual variations, including large-scale effects relating to El Niño/Southern Oscillation dynamics and smaller-scale fronts and eddies [*Marchesiello et al.*, 2003].

[3] On the west coast of the United States, the effects of topography and instabilities play important roles in the alongshore coastal jets and the offshore Ekman transport [*Narimousa and Maxworthy*, 1989; *Batteen*, 1997; *Tseng and Ferziger*, 2001; *Marchesiello et al.*, 2003]. The topographic effect on the wind-driven coastal circulation has been shown by *Narimousa and Maxworthy* [1989] to form local upwelling centers and standing waves with offshore Ekman transport. The upwelling is forced by the prevailing alongshore winds, which are enhanced by coastal mountain ranges and seasonal stratification to produce a strong low-level atmospheric jet [*Haney et al.*, 2001]. These winds force a surface Ekman transport to the right, i.e., in the offshore direction. Upwelling is a three-dimensional flow in which buoyancy, rotation, stratification and surface forcing are all significant, and it plays an important role in the biology of the coastal environment. The "upwelled" water occurs as a cool band along the coast, typically tens of kilometers wide, and is separated from the warmer offshore waters by a series of fronts, plumes and eddies extending more than 100 km offshore. Away from the coast, an Ekman layer develops in the upper ocean. The depth of this layer varies, but it has strong vertical shear. Attention has focused on the upwelling plume, or filament, extending from Point Sur [*Traganza et al.*, 1980; *Chelton*, 1984; *Breaker and Mooers*, 1986].

[4] *Rosenfeld et al.* [1994] studied the circulation in the vicinity of Monterey Bay during the upwelling season (i.e., spring and summer) when strong upwelling-favorable (equatorward alongshore) winds result in strong near-surface horizontal temperature gradients and great biological productivity. This upwelling phenomenon is confined to a narrow region adjacent to the coast [*Ramp et al.*, 1997]. Other coastal upwelling through positive wind stress curl and deep upwelling also contribute significantly to the upwelled water found in the Monterey Bay [*Breaker and Broenkow*, 1994]. All of these processes affect the regional circulation in the Monterey Bay area. Besides, the existence of Monterey Submarine Canyon (MSC) complicates the general circulation in the region. MSC is the major topographic feature with steep bathymetry inside Monterey Bay. The deep currents of Monterey Bay are not well understood. The flow is thought to be primarily up-canyon at depth, with across canyon currents with different directions depending on the depth [*Breaker and Broenkow*, 1994].

[5] Since the regional circulation in the Monterey Bay area is tightly influenced by the complex topography (e.g., MSC, Sur Ridge, etc.) and highly correlated to the coastal upwelling along the west coast of the United States, it is very challenging to simulate the circulation in this area numerically. The Princeton Ocean Model (POM) developed by *Blumberg and Mellor* [1987] is widely used for studying the coastal ocean, and has been used to simulate this region [*Lewis et al.*, 1998; *Ly and Luong*, 1999; *Petruncio et al.*, 2002; *Shulman et al.*, 2002]. The modeling studies in this region have mostly used simplified dynamics, domains, and forcing, with coarse spatial resolution or/and short integration times. *Shulman et al.* [2002] developed a high-resolution, data-assimilating POM of Monterey Bay used in the Innovative Coastal-Ocean Observing Network (ICON). Their simulation employed realistic wind forcing and surface conditions [*Shulman et al.*, 2002; *Paduan and Shulman*, 2004] and was used to hindcast the regional circulation of Monterey Bay. The model adopted a data assimilation scheme to improve both the correlation between the ICON model and the observed currents and the predicted location and intensity of upwelling events. Recently, *Chao et al.* [2002] presented a high-resolution simulation in this region using Regional Ocean Model system (ROMS). Unfortunately, POM and ROMS use σ-coordinate system in the vertical while there are often problems with the σ-coordinate over relatively steep bathymetry with realistic temperature and salinity fields [*Haney*, 1991; *Lewis et al.*, 1998; *Allen et al.*, 2003]. It is well known that MSC is a typical area with steep bathymetric features.

[6] In all of the above numerical approaches, the hydrostatic (HY) primitive equations are used. However, non-hydrostatic (NHY) terms may become significant for features whose horizontal scale is not large compared to their vertical scale; these features may have significant vertical acceleration. In addition, the horizontal scale of the vertical velocity tends to be even smaller than that of other fields because, even in quasi-geostrophic dynamics, it is nonlinearly related to density (through the quasi-geostrophic Ω equation). It becomes likely that the vertical acceleration is not small compared to the buoyancy term; in such cases, there may be significant NHY effects on horizontal velocity through vortex stretching as well as vertical velocity, as found by *Casulli and Stelling* [1998]. However, it is still not clear how the NHY terms affect the circulation in a coastal region with complex bathymetry and upwelling. *Casulli and Stelling* [1998] assessed the effects of the HY approximation in various applications and found

that the HY model is not accurate in some cases. The HY approximation breaks down when the vertical acceleration is significant compared to the buoyancy force.

[7] Thus the response to small-scale bathymetric features may be significantly NHY. NHY effects may be significant whenever the Rossby radius of deformation is small, as it is for surface-trapped fronts and frontal eddies near the surface due to the winter storm events, which generally have small horizontal scales. Vertical acceleration associated with the bores produced by internal wave reflection at topography is also poorly represented by the HY model [*Rosenfeld et al.*, 1999; *Legg and Adcroft*, 2003]. In realistic topography, along-slope tides produce internal hydraulic jumps and solitary wave packets as they flow over corrugations. This is not well represented by HY models.

[8] In this paper, we use a high-resolution numerical model to simulate a coastal area in which the dynamics are determined by the complex geometry of a coastline, steep bathymetry, and the influence of the water masses that constitute the CCS. The bottom bathymetry is accurately represented using the ghost cell immersed boundary method, GC-IBM [*Tseng and Ferziger*, 2003, 2004]. Our goal is to simulate the regional-scale ocean response with realistic dynamics (annual cycle), forcing and domain. In particular, we focus on NHY effects (by comparing the results of HY and NHY models) and the role of complex geometry, i.e., the bay and MSC, on the nearshore circulation. To the best of our knowledge, the current study is the first to simulate the regional circulation in the vicinity of Monterey Bay using a NHY model. This paper is organized as follows. Section 2 introduces the high-resolution Monterey Bay Area Regional Model (MBARM). Section 3 provides the general description and comparison with observation data. Section 4 compares the results of HY and NHY models. Section 5 quantifies the NHY effects. Finally, conclusions are drawn in section 6.

2. Monterey Bay Area Regional Model (MBARM)

[9] In order to accurately study the regional circulation in the vicinity of Monterey Bay, we used the nonhydrostatic, z-level, mixed Arakawa A and C grid, fourth-order accurate Dietrich/Center for Air-Sea Technology (DieCAST) ocean model, which provides high computational accuracy and low numerical dissipation and dispersion [*Dietrich et al.*, 2004a]. The Monterey Bay Area Regional Model (MBARM) is one-way coupled to a large-scale California Current System DieCAST model and uses the GC-IBM [*Tseng and Ferziger*, 2003, 2004] to represent the coastal geometry and bathymetry in the local model.

2.1. Governing Equations

[10] The governing equations are as follows:

Conservation of mass:

$$\nabla \cdot \mathbf{V} = 0 \tag{1}$$

Momentum equations:

$$\frac{\partial u}{\partial t} = -\nabla \cdot u\mathbf{V} + fv - \frac{1}{\rho_0}\frac{\partial p}{\partial x} + \nabla_h \cdot A_h \nabla_h u + \frac{\partial}{\partial z}\left(A_v \frac{\partial u}{\partial z}\right) \tag{2}$$

$$\frac{\partial v}{\partial t} = -\nabla \cdot v\mathbf{V} - fu - \frac{1}{\rho_0}\frac{\partial p}{\partial y} + \nabla_h \cdot A_h \nabla_h v + \frac{\partial}{\partial z}\left(A_v \frac{\partial v}{\partial z}\right) \tag{3}$$

$$\frac{\partial w}{\partial t} = -\nabla \cdot w\mathbf{V} - \frac{1}{\rho_0}\frac{\partial p}{\partial z} + \nabla_h \cdot A_h \nabla_h w + \frac{\partial}{\partial z}\left(A_v \frac{\partial w}{\partial z}\right) - \left(\frac{\rho - \overline{\rho}}{\rho_0}\right)g \tag{4}$$

Conservation of scalar (salt or potential temperature):

$$\frac{\partial S}{\partial t} = -\nabla \cdot S\mathbf{V} + \nabla_h \cdot K_h \nabla_h S + \frac{\partial}{\partial z}\left(K_v \frac{\partial S}{\partial z}\right) \tag{5}$$

Equation of state:

$$\rho = \rho(S, T) \tag{6}$$

where u and v are the x and y components of velocity vector $\mathbf{V} = (u, v, w)$ respectively; f is the Coriolis parameter; ρ_0 is the background density; $\overline{\rho}$ is the horizontally averaged density at depth z; p is the pressure; A_h, A_v are the horizontal and vertical eddy viscosity respectively; S is the salinity; T is the potential temperature; K_h, K_v are the horizontal and vertical eddy diffusivity respectively.

2.2. Model Description

[11] The model uses a blend of collocated and staggered grids structures (Arakawa A and C grids). The Coriolis terms are evaluated on the "a" grid and thus have no spatial interpolation error, which is a significant advantage for a dominant term [*Dietrich*, 1997]. We include the local variation of the Coriolis parameter f in this region (although the variation is not significant) so that it is consistent with the coupled large-scale CCS model [*Haney et al.*, 2001]. The numerical procedures are detailed by *Dietrich and Lin* [2002] and *Tseng* [2003]. Herein, we compare results from HY and NHY versions of DieCAST model applied to Monterey Bay in order to determine NHY effects. The nonhydrostatic model better resolves the vertical component without convective parameterization [*Dietrich and Lin*, 2002]. The only difference between the HY and NHY MBARM models is the way we obtain the vertical velocity component. The NHY model solves equation (4) iteratively [*Dietrich and Lin*, 2002] while the HY model obtains the vertical velocity diagnostically from the continuity equation [*Dietrich*, 1997; *Dietrich et al.*, 1987].

[12] Fourth-order central differencing is used in the control volume approximation to compute all advection and pressure gradient terms, except adjacent to boundaries where second-order accuracy is used [*Sanderson and Brassington*, 1998]. The current fourth-order, nondissipative advection scheme greatly reduces or eliminates numerical dispersion (overshoots), which may appear in the region where the flow is not fully resolved. Such overshoots (oscillations) can be further eliminated by a coordinate invariant streamwise upwind formulation for advection without degrading the high-order accuracy [*Ferziger and Tseng*, 2004]. However, the upwind-biased method is not adopted here in order to avoid its artificial contribution to mixing in the ocean [*Tseng and Dietrich*, 2005]. Excessive mixing is undesirable in the nearly inviscid, adiabatic flows that dominate the ocean circulation outside the thin surface and bottom mixed layers.

[13] The conservation laws (momentum, energy, salinity and incompressibility approximation to mass conservation) are all applied to the same (collocated, nonstaggered) set of control volumes. This avoids the large numerical dispersion associated with Coriolis term evaluation on staggered grids. These equations describe the evolution of control volume averaged quantities, and involve fluxes of conserved quantities across the control volume faces. These fluxes and the horizontal pressure gradient are all evaluated in terms of the predicted control volume averages using fourth-order-accurate approximations [*Sanderson and Brassington*, 1998].

[14] *Sanderson and Brassington* [1998] presented a detailed analysis of the accuracy of the DieCAST model. *Sanderson* [1998] further discussed the rationale for using higher-resolution and higher-order numerics. He used a scaling analysis and numerical examples to explore the gains in accuracy achieved by grid refinement and increased order of differencing operators. The most computationally efficient strategy for achieving accuracy required fourth-order differencing schemes.

[15] The model uses a rigid lid approximation, which has been shown appropriate for "slow modes" general circulation [*Smith et al.*, 1992; *Dukowicz et al.*, 1993]. At the regional ocean scale, the "slow modes" (low-frequency, long-timescale motion) dominate ocean circulation. Using a rigid lid excludes the "fast modes" associated with barotropic free surface waves. Free-surface "fast modes" lead to very little net material displacement over timescales long compared to their period. For the slow modes that dominate the ocean circulation, the surface elevation field may be derived from the model-determined sea surface pressure at the rigid lid. The surface height signal of the slow modes is almost identical to that inferred from the pressure against the rigid lid [*Smith et al.*, 1992; *Dukowicz et al.*, 1993]. *Staneva et al.* [2001] showed that the hydrostatically equivalent sea surface height (SSH) determined by a rigid lid model matched well with the free surface height measured from the remote sensing data after temporal filtering its fast modes. The rigid lid approximation does not affect internal gravity wave speeds. Thus it does not affect geostrophic adjustment of the baroclinic mode that dominates the general circulation. The rigid lid approximation also simplifies the treatment of open boundaries because it greatly reduces the range of frequencies that must be addressed. This constraint can be easily relaxed later by using a free surface to take the effects of waves into account. We concentrate the current study on the slow mode circulation. A free-surface version of the current model has been used to study an idealized internal tide generation over sloping bathymetry [*Lu et al.*, 2001].

[16] The Poisson equation is solved by an efficient error vector propagation (EVP) elliptic solver [*Roache*, 1995]. Density is determined from a nonlinear equation of state relating density to potential temperature, salinity and pressure. We present the MBARM results with realistic coastal bathymetry without smoothing.

2.3. Model Implementation

[17] The domain of MBARM extends from 36.1° to 37.4°N and from the California coast out to 122.9°W (Figure 2); the horizontal grid size is uniformly 1/72° (≈1.5 km) for the medium grid (Figure 2), and 1/108° (≈1 km) for the fine grid. The vertical grid has 28 nonuniformly spaced levels. The surface buoyancy flux is computed by nudging both the temperature and the salinity toward *Levitus*' [1982] monthly climatology. This is almost equivalent to adding heat and/or freshwater to the top layer. This salinity condition, although widely used, has little physical basis and does not conserve salt material exactly [*Dietrich et al.*, 2004b], but it has little effect in the region modeled because the salinity field is strongly constrained by the open boundary inflows; freshwater sources from rivers and precipitation, and sinks from evaporation have only minor effect in this region. The wind stress is from *Hellerman and Rosenstein*'s [1983] 1° × 1° monthly climatology for consistency with the coupled CCS model [*Haney et al.*, 2001]. The southeastward winds intensify during spring and summer and weaken during fall and winter. The vertical viscosity and diffusivity are based on the scheme proposed by *Pacanowski and Philander* [1981]. The horizontal eddy viscosity and diffusivity are 20 m^2/s. This gives a damping time of nearly a month for disturbances of size 10 km.

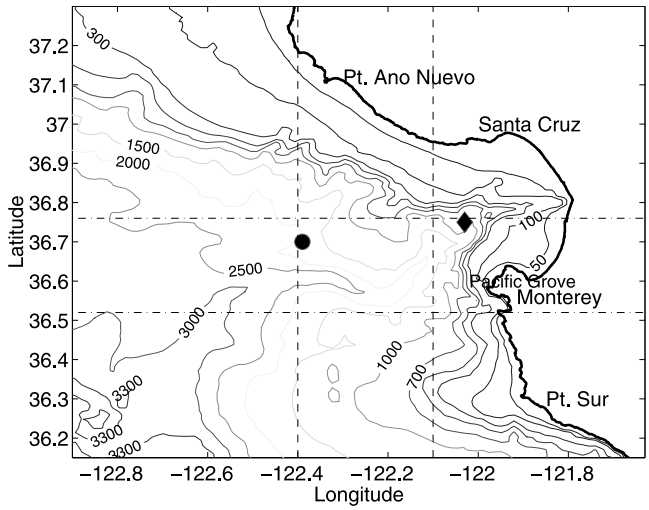

Figure 2. Model domain of Monterey Bay area and bathymetry. Locations of moorings M1 and M2 are marked by a diamond and a circle, respectively. Dash-dotted lines, latitudes 36.52°N and 36.76°N; dashed lines, longitudes 122.4°W and 121.1°W. The lateral boundary region matching the depths between coarse and fine grids is not shown (see section 2.5 for detailed discussion). See color version of this figure in the HTML.

[18] Bathymetry is unfiltered U.S. Geological Survey 250 m resolution topography [*Wong and Eittreim*, 2001]. The bathymetry filters used in some models would result in underprediction of the intensity of the coastal current. The bottom topography and the coastal geometry are adequately represented by the immersed boundary module [*Tseng and Ferziger*, 2003]. The sea floor is insulated and partial slip as parameterized by a bottom drag coefficient of 0.002. Significant momentum exchange with the California Current occurs through the open boundary; these are discussed in the next sections.

2.4. Ghost Cell Immersed Boundary Method (GC-IBM)

[19] The GC-IBM specifies a body force in such a way as to simulate the presence of bottom topography accurately instead of stair-step approximation in a *z*-level model. A

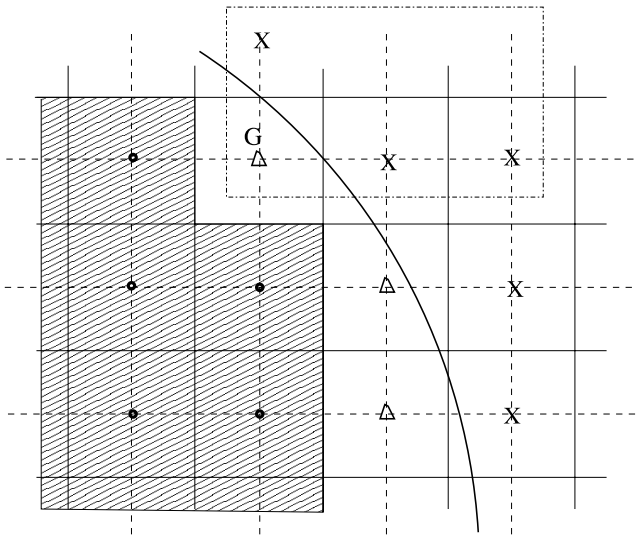

Figure 3. Schematic of computational domain with an immersed boundary. The physical boundary is represented by a curved line. Crosses, point in the physical domain; triangles, the ghost cell domain.

detailed description of the methodology and the systematic treatment of various boundary conditions are given by *Tseng and Ferziger* [2003]. This approach is developed through use of a ghost zone. In order to represent the complex boundary on a Cartesian grid, a boundary forcing term F_i is added to the momentum equation implicitly through ghost cells [*Tseng and Ferziger*, 2003]. The immersed boundary and a ghost cell zone are illustrated in Figure 3. We express the flow variables in terms of a polynomial and use it to evaluate the ghost point values. Therefore the variables in the ghost zone vary on the basis of the local topography instead of masking them in the stair-step approximation. We use linear and quadratic approaches which preserve the second-order accuracy of the overall numerical scheme [*Tseng and Ferziger*, 2003]. The scheme is equally applicable to steady bottom topography and moving boundary problems.

2.5. Open Boundary Treatment

[20] At present, one of the greatest limitations in regional modeling is the open boundary conditions (OBCs). The currents in the vicinity of Monterey Bay and the offshore CC have distinctive spatial scales, $O(1-10)$ km versus $O(100-1000)$ km. In order to focus on the regional circulation without extremely intense computational resources, we have to couple the region to the larger scale through an open boundary. The open boundary should allow perturbations generated inside the computational domain to leave it without deterioration of the inner model solution and allow physically important external information to advect inward.

[21] The rigid lid approximation simplifies the treatment of open boundaries by greatly reducing the range of frequencies that must be addressed. The Orlanski-like radiative approximation is excellent when dealing with a single dominant phase speed [*Orlanski*, 1976]. The Orlanski radiation condition solves a one-dimensional wave equation at the boundary, thus allowing waves to propagate out of the domain, but it is not accurate when a wide range of phase speeds must be addressed. A simple upwind open boundary treatment works nicely in some models, including DieCAST [*Haney et al.*, 2001; *Dietrich*, 1997].

[22] The model is one-way coupled from a large-scale CCS model [*Haney et al.*, 2001] that has resolution 1/12°. In order to simplify the analysis and minimize the effects of open boundary on HY and NHY comparison, the year 3 result from large-scale CCS model [*Haney et al.*, 2001] is used to force the open boundary annually and all quantities are interpolated from daily CCS model output and updated every time step (40 s). Figure 4 shows the hydrostatic equivalent SSH on the day 150 of year 3 from the large-scale CCS model result. A large amount of mesoscale eddies and meanders are observed in Figure 4. The same monthly, climatological forcing is used in the CCS model. The MBARM is initialized by interpolation of the coarse CCS model results after two years of CCS simulation. A schematic diagram of the grid arrangement for the one-way nesting is shown in Figure 5.

[23] All open boundary conditions are based on boundary fluxes. A pure upwind advective scheme is used at the three lateral open boundaries (north, south, and west) for all variables. The normal boundary advective flux is expressed as

$$F_n = U_n \frac{\partial \phi}{\partial n} \tag{7}$$

where

$$\frac{\partial \phi}{\partial n} = \begin{cases} (\phi - \phi_o)/\Delta x_n & U_n \geq 0 \\ (\phi_i - \phi)/\Delta x_n & U_n < 0 \end{cases} \tag{8}$$

and U_n is the normal velocity on the open boundary specified from the CCS model. ϕ represents any of the three velocity components, temperature or salinity at the boundary. ϕ_o is the variable on the open boundary obtained from the CCS model and ϕ_i is the variable at one grid point inside the open boundary, Δx_n is the grid spacing in the direction normal to the boundary. Thus large-scale data are advected inward at an inflow boundary and the interior data is advected outward at

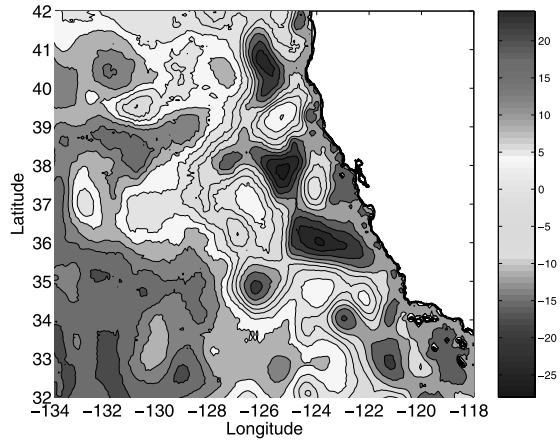

Figure 4. Hydrostatic equivalent sea surface height (SSH) on day 150 of year 3 from the large-scale CCS model. See color version of this figure in the HTML.

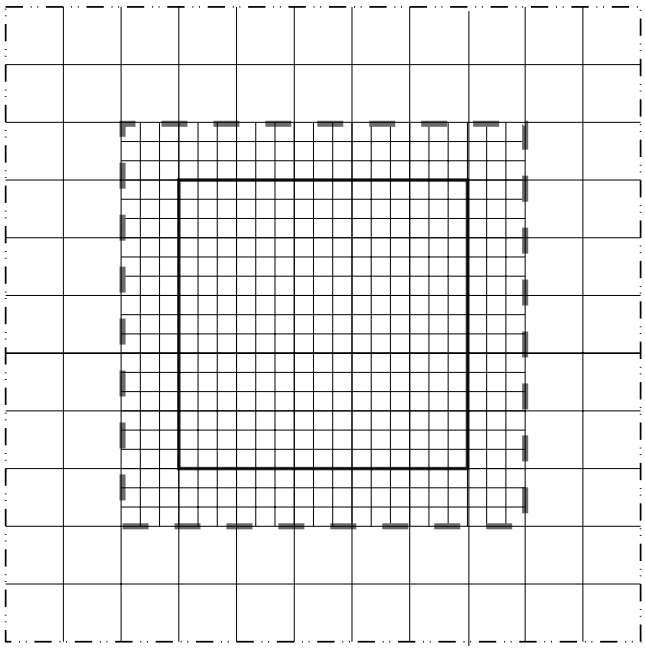

Figure 5. Schematic diagram of grid arrangement for the nesting. Both coarse (larger domain) and fine (smaller domain) grids are shown. The simulation domain is bounded by the outer dash-dotted line. There is an intermediate region where the depth is smoothed to match the different depths between these two grids (bounded by the solid and dashed lines). See color version of this figure in the HTML.

an outflow boundary. The net lateral boundary flow through the open boundary is adjusted at every time step at the open boundary. This insures there is no net inflow into the modeled region and is required by incompressibility. It has been argued that the hydrostatic, primitive equations are ill posed when an inappropriate open boundary condition is used. The ill-posedness implies no single set of boundary conditions can be defined to guarantee existence of a stable, unique solution. If the proper number of boundary conditions is not specified, the solution of the primitive equations will lead to the exponential growth of energy and numerical instability [*Oliger and Sundstrom*, 1978]. According to *Oliger and Sundstrom* [1978] and *Mahadevan et al.* [1996], the numerical problem is well posed if the velocity vector, salinity, and temperature are specified at the inflow boundary condition and the normal velocity is specified at the outflow boundary. The above open boundary treatment satisfies these requirements and is well posed in either HY or NHY formulation. The ill-posedness due to overspecification of boundary condition in the primitive equation model typically leads to the energy growth of the system [*Oliger and Sundstrom*, 1978]. We do not observe this unphysical energy growth in either HY or NHY model for long time integration (>70 years). Note that the current MBARM models do not use sponge layers, which dissipate the errors generated by the overspecification of boundary conditions in most ocean models. The current open boundary treatment in a primitive equation has been used for two-way coupling in a North Atlantic ocean model to investigate the nonlinear dynamics of Gulf stream separation [*Dietrich et al.*, 2004a]. The two-way coupling, multigrid treatment is currently extended to a Mediterranean Sea/North Atlantic coupled model which includes six simulation domains. No ill-posedness is found. *Palma and Matano* [2000] investigated the performance of combinations of OBCs using POM. They found that the best overall performance of OBCs was a flow relaxation scheme for barotropic modes, a radiation condition for baroclinic modes, and combined advection and relaxation for the scalar field. In fact, the current scheme corresponds to a simplified version of the scheme suggested by *Palma and Matano* [2000].

3. Simulation Results

3.1. Grid Sensitivity Study

[24] We performed a grid sensitivity study to assess the effects of grid resolution on the NHY simulation results. A finer grid 1/108° (1 km) and a coarser grid 1/36° (3 km) resolutions were used in addition to the medium grid 1/72° (1.5 km) resolution. The number of vertical layers was not changed in order to match the lateral open boundary data from the larger-scale simulation. The hydrostatic equivalent SSH and mean velocity field at depth 10.1 m for medium and finer grids during May from the second year are shown in Figure 6.

[25] The medium and fine resolution simulations exhibit very similar patterns inshore and offshore, including the region close to where the lateral OBCs are applied. Only little difference is found close to the coast, showing that the medium 1/72° resolution results converge well to the finer resolution ones. The coarser grid 1/36° resolution result is not shown here because of its lack of convergence. The regional circulation is tightly coupled to the large-scale CCS model (Figure 4). These show that the OBCs are adequately imposed and that offshore eddies can be fully resolved using the medium 1/72° resolution.

3.2. Equilibrium State

[26] The model is initialized by the coarse CCS model and then run for 9 years. The volume-integrated kinetic energy (KE) and surface KE are shown in Figure 7. It is clear that the surface kinetic energy and volume integrated KE oscillates quasiperiodically after 100 days. The global kinetic energy levels are consistent with the dominant annual cycle climatology and yearly repeating open boundary conditions from the CCS model [*Haney et al.*, 2001]. The kinetic energy converges to its equilibrium state very quickly and shows that the model is tightly coupled to the large-scale forcing. The KE reaches its peak energy level during summer period, which is caused directly by the upwelling favorable, equatorward wind. The seasonal variation is clearly seen in the time series KE.

[27] Although the KE shows quasi-equilibrium behavior in the MBARM model, interannual variability is also present. We further analyze the intrinsic variability by presenting time series of surface longitudinal velocity (Figures 8a and 8c) and vertical vorticity (Figures 8b and 8d) for each year at two different locations. Figures 8a and 8b are located near southern lateral boundary (121.1°W, 36.14°N) while Figures 8c and 8d are located at the center of simulation domain (122.45°W, 36.61°N). Time series for each year (year 2 to year 9) are shown as thin solid lines, with the mean of these time series overlain as a thick solid

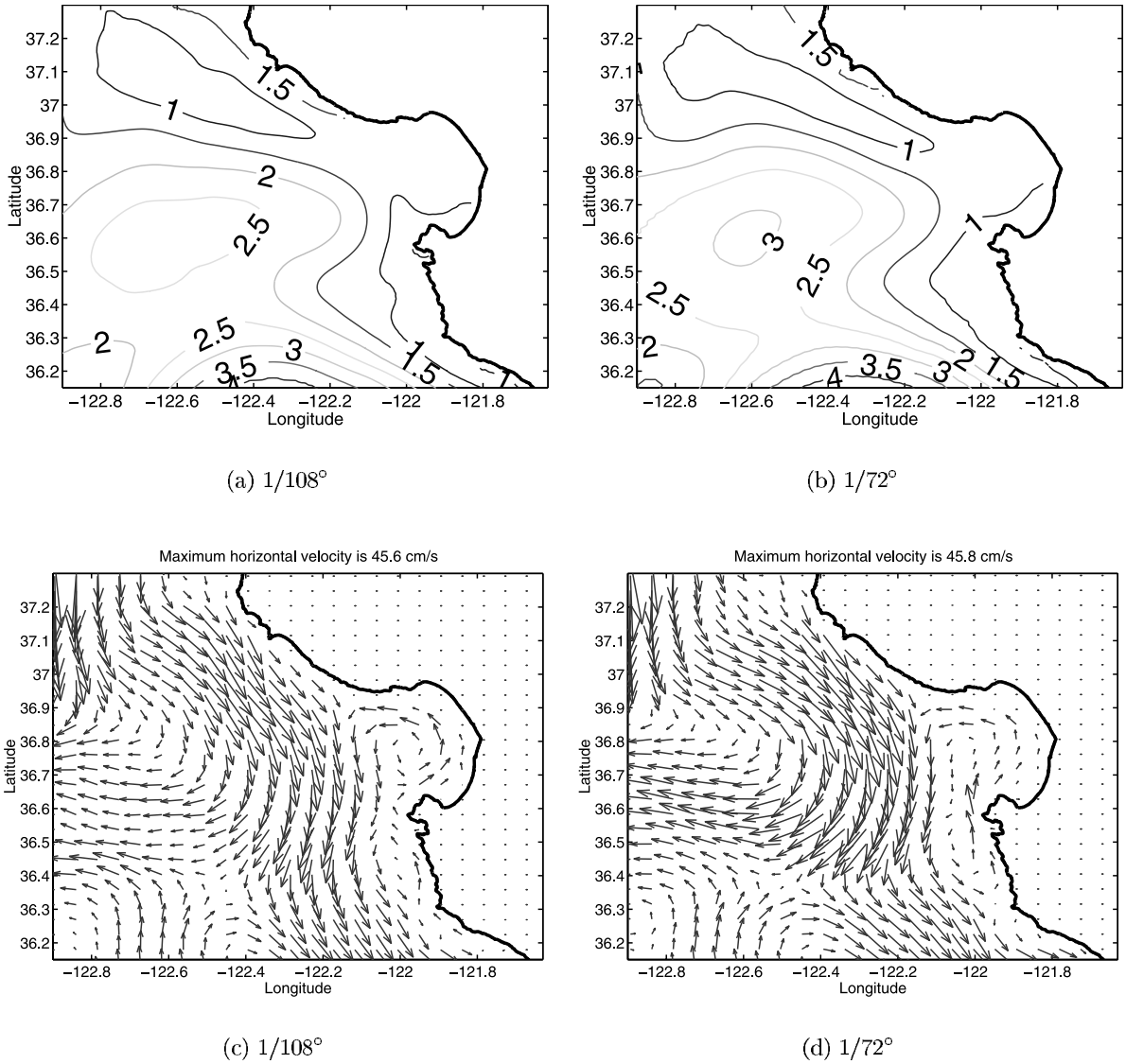

(a) 1/108° (b) 1/72°

(c) 1/108° (d) 1/72°

Figure 6. Grid sensitivity study using a high-resolution grid 1/108° (every third grid is shown) and a medium grid 1/72° (every second grid is shown) from May of year 2. (a and b) Hydrostatic equivalent SSH. (c and d) Mean velocity fields at depth 10.1 m. See color version of this figure in the HTML.

line (every tenth day is plotted). Seasonal variation is clearly shown from these two representative locations. Time series from the large-scale CCS model result (at the same locations) are also shown on the same plots by thick dash lines (every 30th day is plotted). The variance between different years is very small in Figures 8a and 8b. The largest variance between different years occurs during spring to summer. The time series are very similar to the trend in the large-scale CCS model. However, the variance between different years is significant in Figures 8c and 8d. The mean time series (think solid lines) are very similar to the annual trend in the large-scale CCS model with large intrinsic/interannual variability. These results show that the MBARM model is strongly forced by the lateral boundary forcing with moderately large intrinsic variability inherent inside the domain. The paths of large mesoscale eddies are similar to those observed in the large-scale CCS model so that the mean pattern is very close to the trend in the CCS model. Only small variance is found close to the lateral boundary while large variance is observed in the domain center and nearshore region.

[28] The spatial distribution of variance of longitudinal velocity and vertical vorticity is shown in Figure 9. The vertical vorticity includes effects of both longitudinal and latitudinal velocities. In Figure 9b, large variance is observed close to the coast, especially near Point Año Nuevo headland. The mesoscale variability is mainly forced by time variability through its lateral boundary conditions from the CCS model. Lateral forcing provides the main source of mesoscale energy and intrinsic/interannual variability is weak in the areas close to the forced boundary. The intrinsic variability is large enough to produce interannual variability in the local domain inside.

[29] The surface temperature from the 220th day (mid-July) of year 6 and year 7 is shown in Figure 10. July is the month having the maximum KE during an annual cycle.

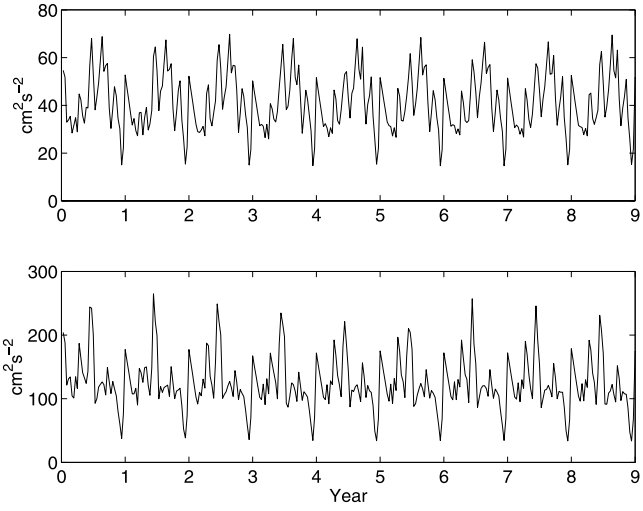

Figure 7. Time evolution of (top) volume-integrated kinetic energy and (bottom) surface kinetic energy for 9 years.

From the two consecutive years, no significant difference is observed in the simulation except the nearshore and center areas. The results are consistent with Figures 8 and 9. Both mesoscale eddies and offshore filaments are found (Figure 10). The intrinsic variability due to mesoscale instabilities is evident in the nearshore region and the eddy fields are energetic. These eddies are possibly generated along the coast through baroclinic instabilities, shear instability and upwelling fronts [*Tseng and Ferziger*, 2001]. The life time of these eddies is usually within a week (Figure 11). In addition, some mesoscale eddies may result from large-scale CCS model through open boundary (Figure 4). Figures 11a–11d show the transient of such a mesoscale eddy coming from the south boundary near Sur Ridge and moving northwestward. These eddies and jets move slowly with Rossby wave propagation and may move further offshore, thus influencing the rest of the domain. *Marchesiello et al.* [2003] observed similar small-scale variability in their simulation, and they attributed these characteristics to upwelling fronts and filament structures whose anticyclonic shear is comparable to Coriolis parameter *f*. They suggested the possibility of a transition regime (Coastal Transition Zone, CTZ) where frontal instabilities start to impact coastal currents and offshore mesoscale eddies. High mesoscale variability, including filaments, eddies, and meandering current or jets, has been observed in CTZ [*Mooers et al.*, 1976; *Mooers and Robinson*, 1984; *Strub et al.*, 1991; *Brink and Cowles*, 1991; *Marchesiello et al.*, 2003]. *Staneva et al.* [2001] found similar behavior in the regions of near-zero absolute vorticity in the wake of the major Crimean peninsula abutment of the Black Sea, where the near-zero absolute vorticity eliminates the rotational constraint of vertical circulations and associated vortex stretching, thereby allowing locally rapid conversion of available potential energy to kinetic energy. The upwelling fronts include complicated mixed barotropic and baroclinic instability and Rayleigh-Taylor instability [*Tadepalli*, 1997; *Tseng and Ferziger*, 2001]. The above instability mechanisms have been investigated and discussed in the past [*Mooers et al.*, 1976; *Narimousa and Maxworthy*, 1991; *Tadepalli*, 1997; *Marchesiello et al.*, 2003]. However, the role of these instabilities and their interactions are not clear yet because of the complexity of the system.

[30] Figures 7–10 show that the equilibrium state is achieved quickly in the current MBARM model after several years. The annual cycle is well reproduced with significant intrinsic variability in the interior of the domain. In the following sections, we focus on detailed results from year 6 and year 7 to be sure the model has been run long enough that the results are independent of the initial state.

3.3. General Description

[31] Using Levitus' surface climatological forcing (temperature and salinity) and Hellerman and Rosenstein's climatological wind stress, the simulation reproduces many important features of the observed annual cycle of the CCS including the strengthening of the equatorward jet in spring and the weakening of the jet in autumn and winter. Coastal eddies occur primarily near some major headlands, especially Point Año Nuevo, Pacific Grove and Point Sur. To examine the general circulation in the vicinity of Monterey Bay, we focus on the annual mean flow after the model reaches the equilibrium state.

[32] The mean velocity fields for a simulation year (year 6) at various depths (10.1, 50, 100, 300, 400, 700 m) are shown in Figure 12. As mentioned in the introduction, the major features in the Monterey Bay area are the shallow, equatorward, broad CC and two narrow poleward boundary currents (CUC and IC) along the coast. It is clear to see CUC at depth. The surface flow is greatly affected by surface wind forcing. Vertical shear layers appear at moderate depth (50–200 m). The mean velocity pattern clearly delineates the extent of poleward flow associated with the inshore currents. The subsurface northward flow exists below depth 300 m and is consistent with the year round northward flow associated with the CUC. The transition from CC to CUC occurs around depth 100–500 m and the strongest CUC occurs at depth 200–300 m, which is consistent with previous observations [*Hickey*, 1979; *Collins et al.*, 2000; *Pierce et al.*, 2000]. These flows are tightly coupled with the large-scale CCS model through open boundary.

[33] In average, a weak cyclonic eddy is observed in the Monterey Bay. The eddy appears frequently inside the bay during spring and summer upwelling seasons. A detailed description of seasonal variation is given by *Tseng* [2003]. There is also a large-scale, anticyclonic eddy around 30 km from the coast that extends down to depth 100 m where the eddy is stretched significantly by the coastal bathymetry and the MSC (Figure 12c).

[34] *Collins et al.* [2000] estimated the upper 1000 m depth-averaged mean velocity on the basis of 19 cruises conducted from April 1988 to April 1991. They reported a west-northwestward (290°T–310°T) flow with a mean speed of 3.7–5.3 cm/s at four inshore stations C1–C4 (at latitude 36.3°N, 33–65 km away from the shore). We estimate the 1-year depth-averaged annual mean flow along the line connecting these four inshore stations. The comparison is shown in Table 1. The mean magnitude (4.7 cm/s) is slightly larger than that predicted by *Shulman et al.* [2002]. The annual mean flow in the current study is in good agreement with observation without data assimilation. The result shows that the current one-way coupling at lateral

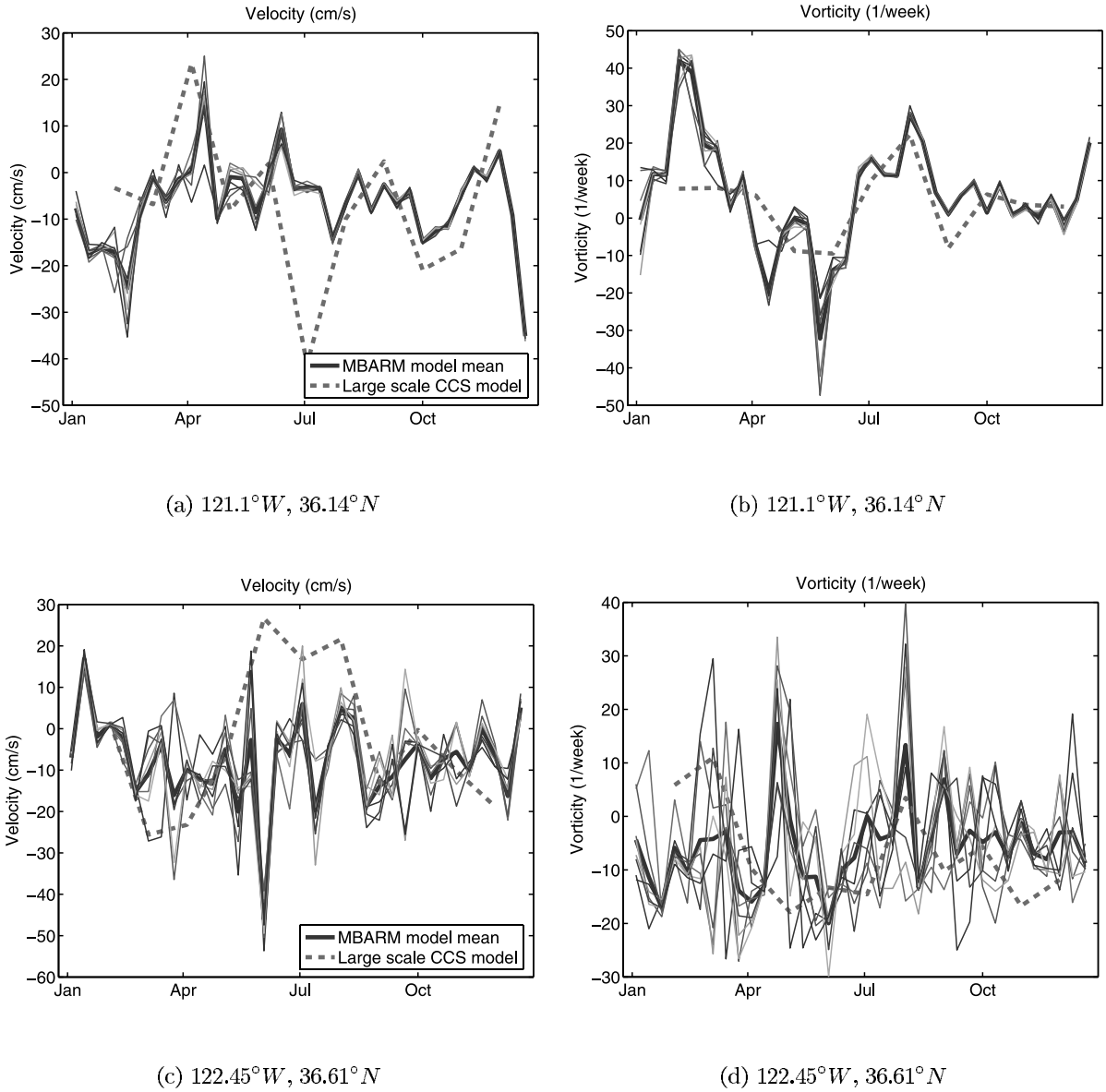

(a) $121.1°W$, $36.14°N$ (b) $121.1°W$, $36.14°N$

(c) $122.45°W$, $36.61°N$ (d) $122.45°W$, $36.61°N$

Figure 8. Time series of surface longitudinal velocity (Figures 8a and 8c) and vertical vorticity (Figures 8b and 8d) within a year at two different locations. Figures 8a and 8b are located at 121.1°W, 36.14°N (near southern boundary). Figures 8c and 8d are located at 122.45°W, 36.61°N (center of domain). Time series for each year (year 2 to year 9) are shown as thin solid lines, with the mean of these time series overlain as a thick solid line. The time series from the large-scale CCS model results are represented by dashed lines. See color version of this figure in the HTML.

boundary and the surface forcing are appropriate to produce correct circulation in this region.

3.4. Comparison With Observation Data

[35] We compare the model temperatures with those measured by Sea-Bird MicroCAT CTDs mounted on MBARI's M1 (122.03°W, 36.75°N) and M2 (122.39°W, 36.70°N) surface moorings (see Figure 2 for the location). Since the model is forced by the average climatology at the sea surface, we do not expect the model to match the observations exactly. In the annual cycle of SST, spring is the coolest time of the year. Spring and early summer are periods of upwelling. The upwelling signal is evident in the currents and the temperature in our simulation. During the late summer and early autumn there are increases in temperature, and intensification of the poleward undercurrent. The seasonal variation is more significant near the surface than at depth. The model results are shown in Figure 13 for the M1 and M2 mooring locations, respectively. The results repeat annually, showing that the model has been run long enough that the results are independent of the initial state. The model results reproduce many of the observed trends. These include the annual variation in temperature, cooling of surface and subsurface temperatures during spring upwelling, warming water masses during summer and early autumn, and slight cooling during late autumn.

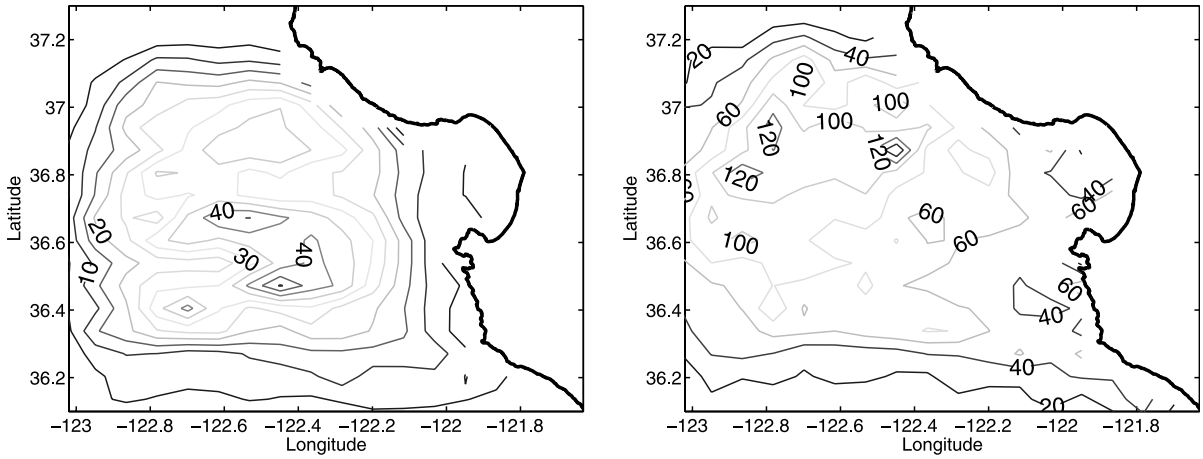

Figure 9. Spatial distribution of variance of (a) longitudinal velocity (cm/s) and (b) vertical vorticity (1/week) in MBARM model. See color version of this figure in the HTML.

[36] The modeled and observed time series of temperatures at the M1 and M2 mooring stations for various depths are presented in Figures 14 and 15, respectively. The modeled time series of temperatures are phased-averaged from year 4 to year 9. We pick two different years of mooring data (year 1995 and year 1999) for comparison. Both years have extensive continuous data without El Niño anomalies. The El Niño anomalies are not included in the climatology forcing. These results display an annual cycle with cold temperatures during upwelling seasons and warmer temperatures during the rest of the year. The near-surface temperature (10 m) at M2 varies between 10° and 15°, which is in the same range as the observations. The temperature at M1 is 1°–2° lower than that at M2, which is again consistent with the measurements. At depth 200 m, the temperature varies from 8° to 9° at both the M1 and M2 stations, consistent with the observational data. However, slightly higher temperature is predicted in the model during spring.

[37] Overall, the model predictions are in reasonable agreement with observations without data assimilation. A more quantitative model-data comparison is made difficult by the existence of interannual variability in both the simulated and observed fields. The most important result of the simulation is the fact that, as in the observation, the annual cycle is evident and well reproduced in the simulation.

[38] During periods of upwelling-favorable winds (spring and summer), there is a band of cold water which flows equatorward across the mouth of Monterey Bay. The upwelling centers are found north and south of Monterey Bay near Point Año Nuevo and Point Sur [*Rosenfeld et al.*, 1994]. Point Año Nuevo has been identified to be the source of cold, salty near-surface water frequently seen in the bay [*Rosenfeld et al.*, 1994]. Within the bay, a cyclonic circulation is often observed [*Breaker and Broenkow*, 1994]. This circulation is observed often in the simulation and is caused mainly by the coastal geometry. Figure 16a shows the monthly averaged simulated surface current in June from year 6 and Figure 16b shows the HF radar-derived velocity fields in June, 1995. The cyclonic circulation within

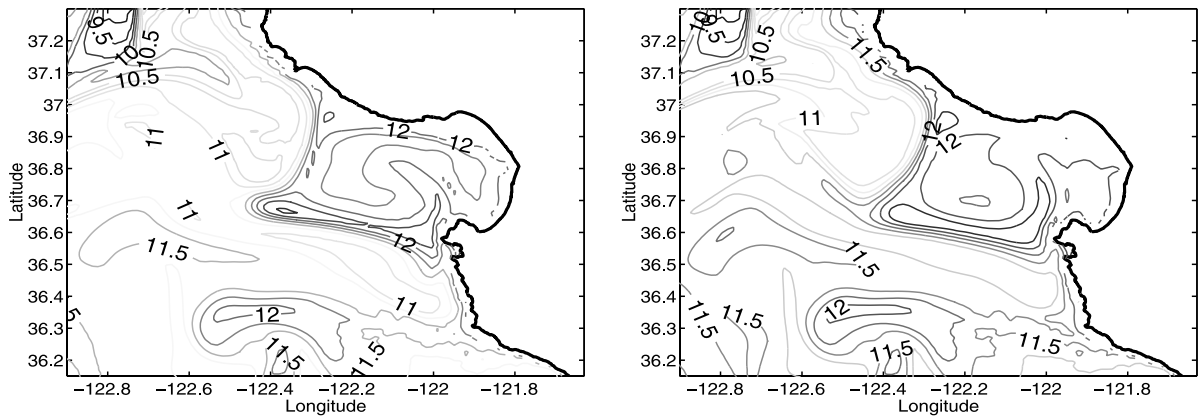

Figure 10. Sea surface temperature (°C) from the 220th day (mid-July) of (a) year 6 and (b) year 7. See color version of this figure in the HTML.

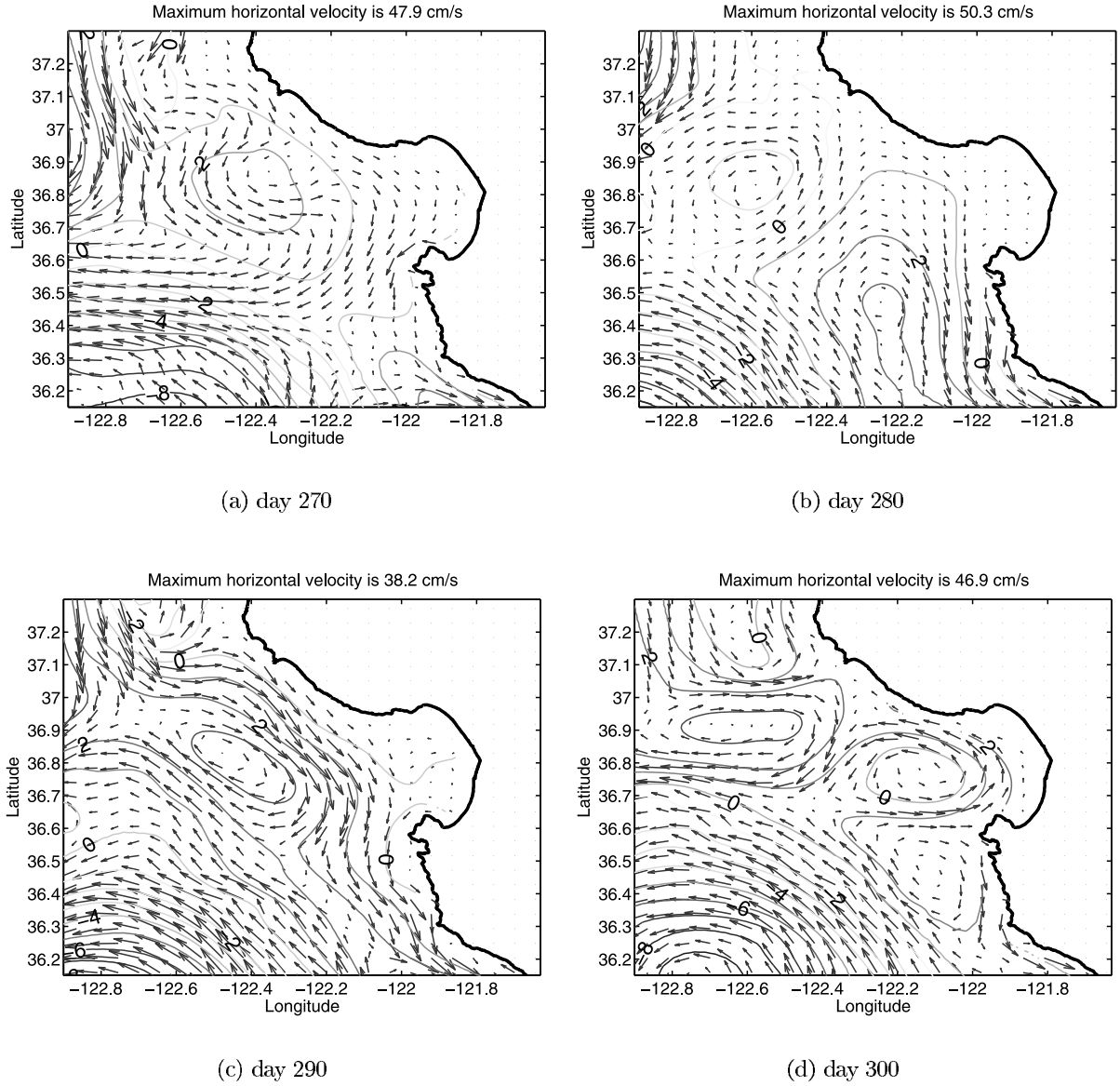

(a) day 270

(b) day 280

(c) day 290

(d) day 300

Figure 11. (a–d) Surface velocity vector and surface pressure (cm) from day 270 to day 300 of year 6 simulation. See color version of this figure in the HTML.

Monterey Bay is consistent with the observed circulation (Figure 16b). HF radar-derived velocity fields during late summer 1992 and 1994 reveal a band of equatorward flow across the mouth of Monterey Bay with cyclonic circulation inside the bay and anticyclonic circulation offshore [*Paduan and Rosenfeld*, 1996]. This feature was also seen in advanced very high resolution radiometer (AVHRR) imagery [*Ramp et al.*, 1997]. The simulation produces patterns very similar to those observed in the HF radar-derived field and satellite images. A warm anticyclone is also apparent in the simulation. Meanders of the California Current with anticyclonic circulation have often been reported [*Breaker and Broenkow*, 1994; *Ramp et al.*, 1997; *Paduan and Rosenfeld*, 1996]. This flow pattern is similar to April-July flow patterns observed in the Monterey Bay area using AVHRR imagery and drifter measurements, and CTD data and Acoustic Doppler Current Profiler (ADCP) observations [*Paduan and Rosenfeld*, 1996; *Rosenfeld et al.*, 1994, 1995]. The equatorward flow across the mouth of Monterey Bay and the cyclonic circulation are seen in our simulation during springtime and are associated with the advection of upwelled water from the Año Nuevo upwelling center [*Rosenfeld et al.*, 1994]. It is shown that irregularities in the coastline geometry are important for "anchoring" upwelling and filaments and enhancing the growth of meanders and eddies. A more detailed investigation of the effects of Monterey Canyon and coastal topography on large-scale circulation is given by *Tseng* [2003].

4. HY Versus NHY Modeling

[39] The growth of meanders and filaments of upwelled water has been demonstrated in many previous studies using HY models. *Chao and Shaw* [2002] studied coastal upwelling meanders and filaments using a NHY model. Their idealized model does not include complex bathymetry,

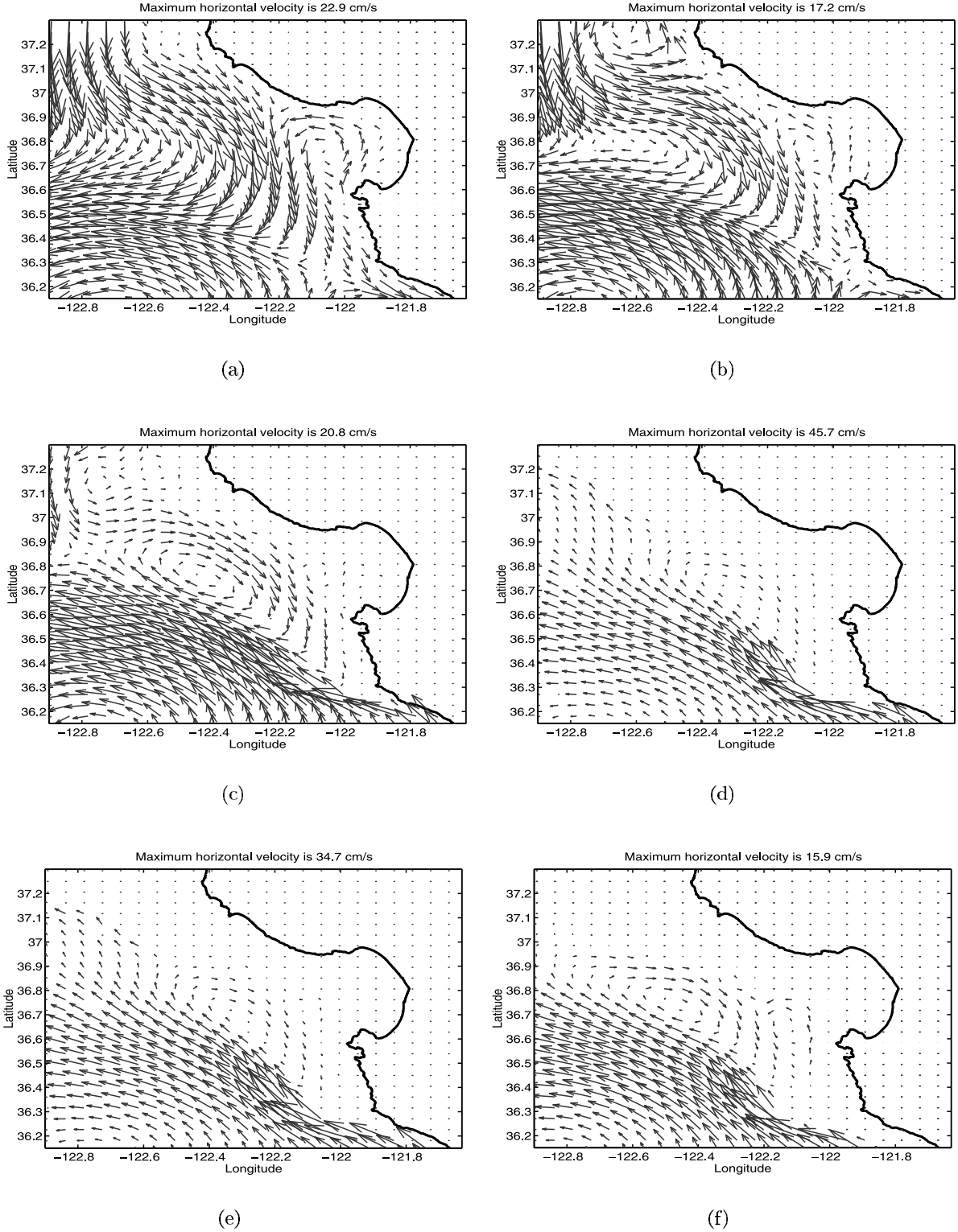

Figure 12. Annual mean velocity field at various depths for a year. At depth (a) 10.1 m, (b) 50 m, (c) 100 m, (d) 300 m, (e) 400 m, and (f) 700 m. See color version of this figure in the HTML.

Table 1. Comparison of Annual Mean Flow

	Depth-Averaged Annual Velocity Magnitude, cm/s	Depth-Averaged Annual Velocity Direction, °T
MBARM results	4.7	301
Numerical results with data assimilation [*Shulman et al.*, 2002]	3.13	308
Observation [*Collins et al.*, 2000]	3.7–5.3	290–310

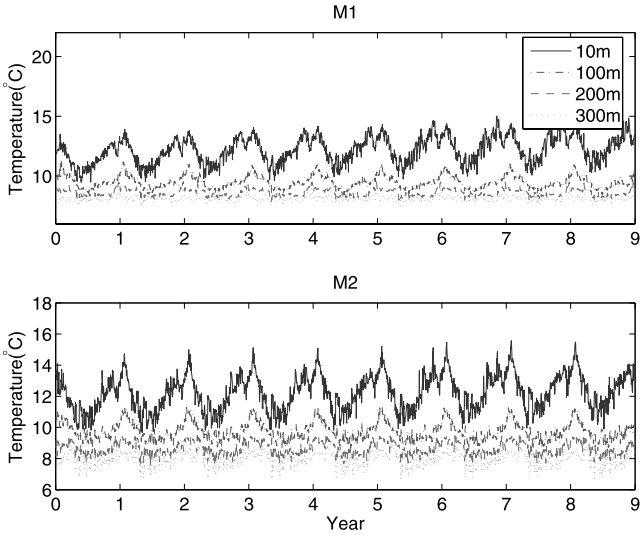

Figure 13. Modeled time series of temperature at stations (top) M1 and (bottom) M2 for nine simulation years. The model repeats smoothly after a year, thus showing that the annual cycle is accurately responded to immediately. See color version of this figure in the HTML.

coastal irregularity or unsteady wind forcing. Their results show that the growth rates of meanders and filaments are enhanced by NHY effects. Here we explore the impact of the HY approximation by comparing results from HY and NHY versions of the DieCAST model applied to Monterey Bay and the surrounding area.

[40] We compare the annual mean velocity field in year 6 from the simulation. The yearly averaged velocity difference ($\overline{\mathbf{V}_d} = \overline{\mathbf{V}_{HY}} - \overline{\mathbf{V}_{NHY}}$) between HY and NHY models at various depths are presented in Figures 17–22. Both horizontal and vertical velocity differences are shown. Significant differences can be observed along the bathymetry and inside Monterey Canyon. The strength of the difference also

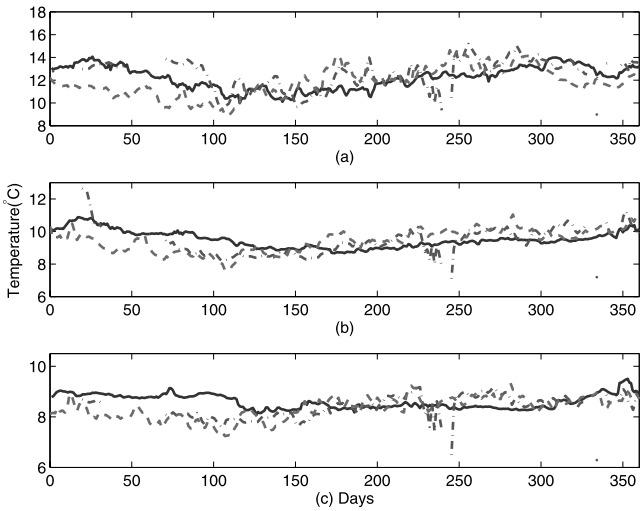

Figure 14. Modeled time series of temperatures (solid lines, 6-year average) and the observed time series of temperature (dash-dotted lines, year 1995; dashed lines, year 1999) at mooring station M1. At depth (a) 10 m, (b) 100 m, and (c) 200 m. See color version of this figure in the HTML.

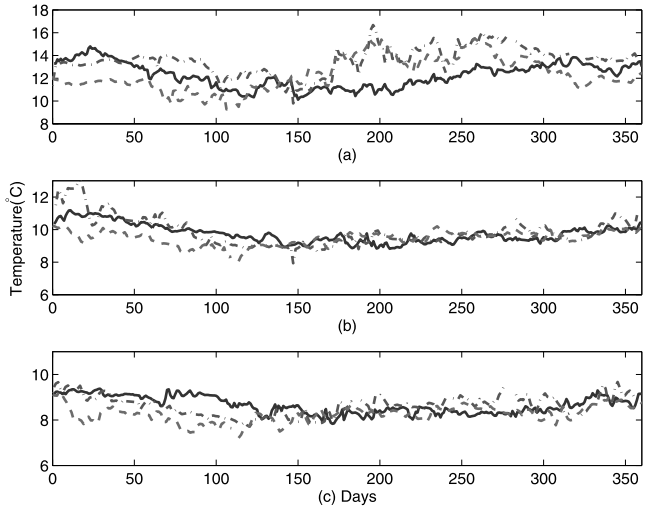

Figure 15. Modeled time series of temperatures (solid lines, 6-year average) and the observed time series of temperature (dash-dotted lines, year 1995; dashed lines, year 1999) at mooring station M2. At depth (a) 10 m, (b) 100 m, and (c) 200 m. See color version of this figure in the HTML.

depends on depth. The deviation of HY from NHY models results from the calculation of vertical velocity [*Dietrich and Lin*, 2002]. The vertical velocity differences between HY and NHY models at various depths are large along the canyon walls at all depths. These results show that rapid changes in slope in the presence of strong flows cause vertical acceleration which violates the HY approximation.

[41] Furthermore, the HY horizontal velocity field also shows a significant departure from NHY prediction in both upper and deep ocean (Figures 17–22). The HY model produces an increased mean cyclonic circulation around 50 km offshore of Monterey Bay at all depths. The velocity difference shows that a strong cyclonic eddy is formed in the domain center, increasing the northward transport across the Monterey Bay due to the stronger undercurrent it generates. The results are consistent with the shifting of correlation between the data-assimilated HY model and surface observation in recent studies [*Paduan and Shulman*, 2004]. The stronger cyclonic circulation in HY model transports inshore eddies further northwestward. Our comparison suggests that the error between the data-assimilated HY model and the observation can be reduced significantly by including the NHY dynamics. The complex nearshore topography enhances the inaccuracy of the HY approximation. The eddy fields at depth in the HY and NHY models are also very different. In particular, significant differences are found near Sur Ridge (water column south of Monterey Canyon between latitudes 36.2°N and 36.4°N) at all depths (Figures 17–22). The most significant velocity difference occurs extensively in this area. Point Sur (see Figure 2 for the location) is the location where the offshore flow is most significant and satellite images also show that filaments occur there frequently [*Rosenfeld et al.*, 1994]. The current comparisons show that the local bathymetry near Point Sur (Sur Ridge) enhances the NHY effects significantly in both shallow and deep regions and these effects cannot be ignored locally. The generation mechanism could be associated with strong CUC flows over sloping bathymetry. These influences include

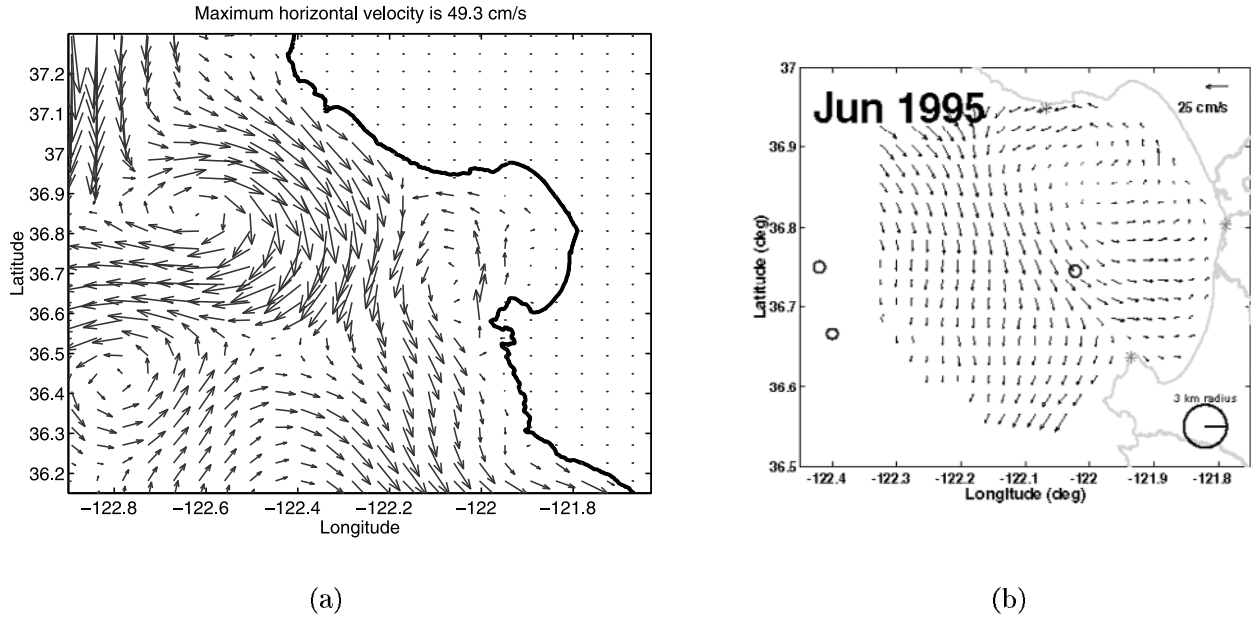

Figure 16. (a) Simulated surface current in June from year 6. (b) Monthly averaged radar-derived current vectors in June 1995 from the Radar and Drifter (RAD) Laboratory at the Naval Postgraduate School. Source: http://www.oc.nps.navy.mil/∼radlab/HFmaps.html. See color version of this figure in the HTML.

the stronger advection into the Monterey Canyon using HY model and the local vertical acceleration which is shown to be important in coastal upwelling. During periods of upwelling-favorable winds (spring and summer), there is a band of cold water which flows equatorward across the mouth of Monterey Bay with typical near-surface speeds of 20–30 cm/s. In summer, the southward flow in the upper ocean strengthens and tends to move offshore, forming the filaments observed in the satellite images. The current simulation suggests that, through NHY feedback, this is an effect of local topography on the enhancement of flow toward bathymetry and the steering effect of the Pacific Grove headland. The same conclusion was suggested by observations [*Ramp et al.*, 1997]. Our results show that NHY effects are important where there are strong inclines in the topography even at depth.

[42] In order to analyze the temporal dependency of the structure in velocity differences, we also compare the velocity difference fields ($\mathbf{V}_d$) from another year. The yearly averaged velocity deviation of HY model from NHY model in year 7 (depth 300 m) is shown in Figure 23. The unreal cyclonic eddy occurs consistently at depth 300 m and other depths in the horizontal velocity difference; and strong deviations in the vertical velocity difference are found along

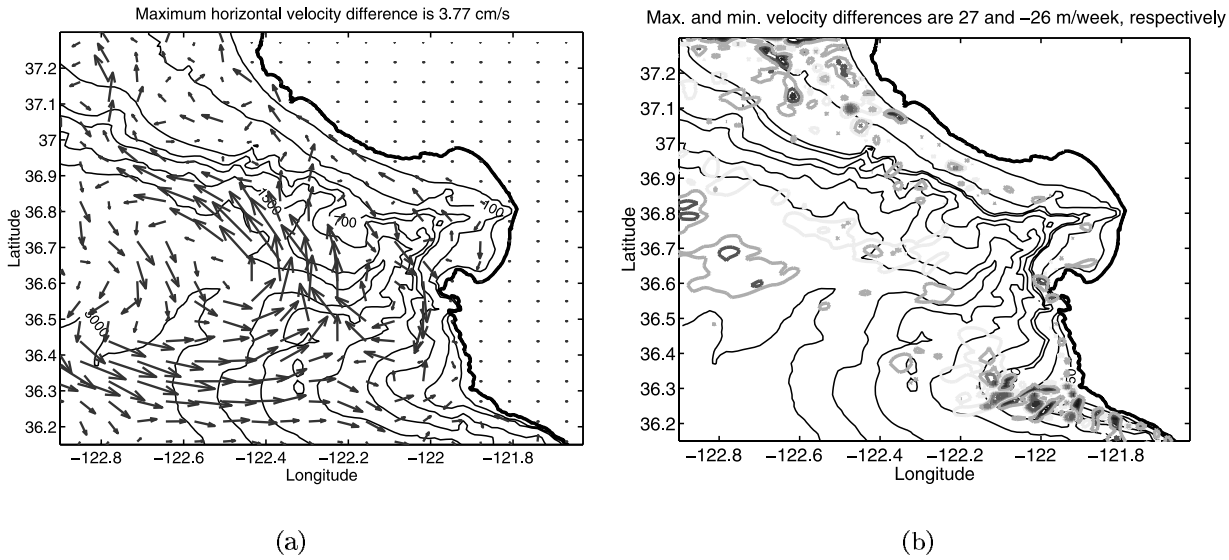

Figure 17. Velocity difference field between HY and NHY models at depth 50 m using the high-resolution MBARM models. The velocity field is yearly averaged from year 6. (a) Horizontal velocity difference and (b) vertical velocity difference contours. See color version of this figure in the HTML.

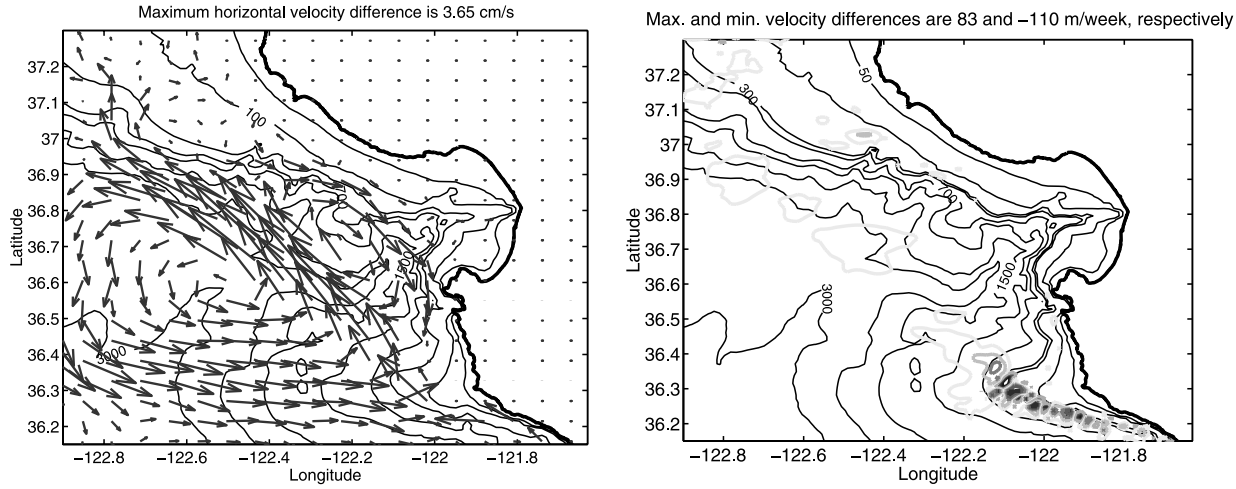

Figure 18. Velocity difference field between HY and NHY models at depth 100 m using the high-resolution MBARM models. The velocity field is yearly averaged from year 6. (a) Horizontal velocity difference and (b) vertical velocity difference contours. See color version of this figure in the HTML.

the coast. These patterns are very coherent. The maximum values again appear in the vicinity of Sur Ridge. All of the velocity components have the same magnitudes as those shown in Figure 19. Only minor differences in the mean velocity deviation are found between year 6 and year 7 and are attributed to interannual variability. The above comparison shows that the deviation structures are very consistent and repeat every year.

[43] In order to further quantify the error introduced by the HY model, we compare the averaged velocity differences between two consecutive years in NHY model at depth 300 m (Figure 24). Figure 24 exhibits randomly distributed, small magnitude, horizontal and vertical velocity components and has totally different patterns from the comparison between HY and NHY models (Figure 19). Quantitatively, the error produced by the HY model is on the order of $O(10)$ larger than small-scale perturbations in the mean velocity distribution.

[44] Finally, we focus on the time series of the spatially averaged velocity deviation between the HY and NHY models (Figure 25). Figure 25 shows time series root mean square (RMS) difference from year 6 to year 8. The time series differences suggest the possible mechanisms that violate the HY approximation. The results show that the deviation of HY model mainly occurs in the strong upwelling season at all depths. The difference in the deep ocean (2000 m) is weak and roughly of the same order of magnitude as the small-scale perturbation. Interestingly, the

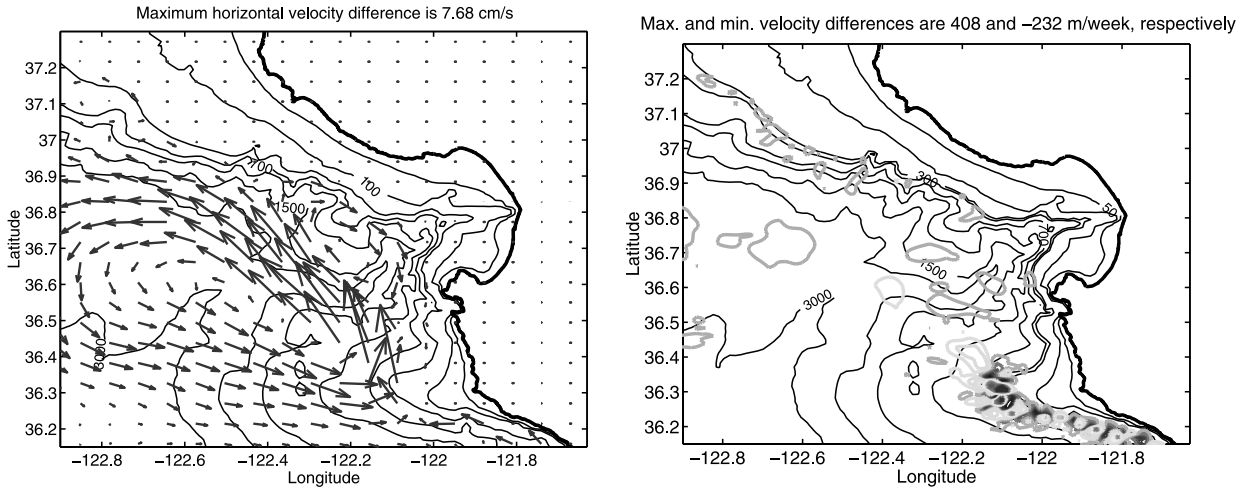

Figure 19. Velocity difference field between HY and NHY models at depth 300 m using the high-resolution MBARM models. The velocity field is yearly averaged from year 6. (a) Horizontal velocity difference and (b) vertical velocity difference contours. See color version of this figure in the HTML.

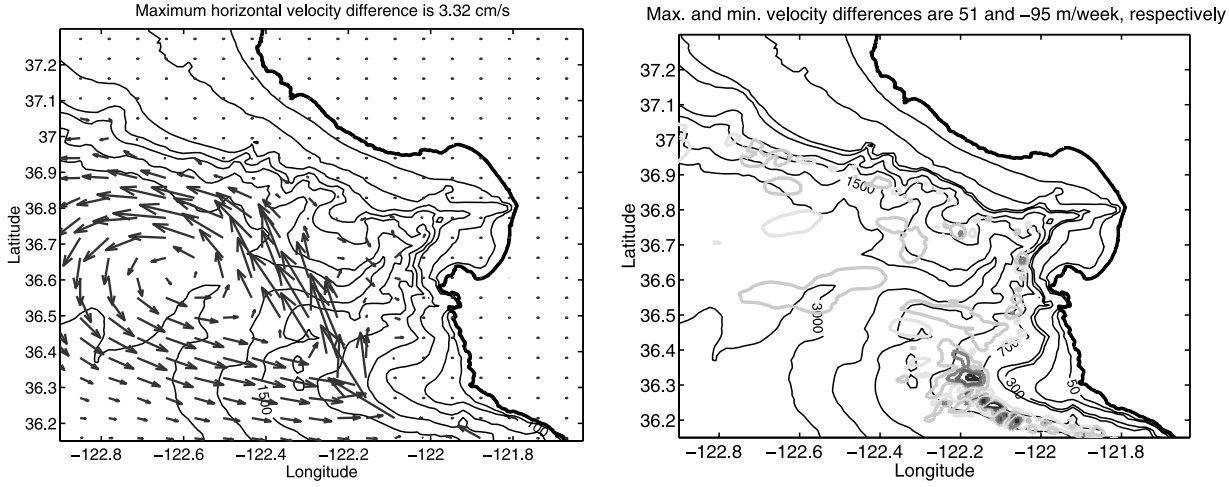

Figure 20. Velocity difference field between HY and NHY models at depth 700 m using the high-resolution MBARM models. The velocity field is yearly averaged from year 6. (a) Horizontal velocity difference and (b) vertical velocity difference contours. See color version of this figure in the HTML.

difference reaches another peak in the near-surface region during winter. In the simulation, the seasonal cycle is characterized by the formation of surface baroclinic jets in the spring of each year shortly after the onset of upwelling-favorable winds [*Tseng*, 2003]. A variety of instabilities subsequently occur along the jet, and the entire field (jets and eddies) propagates offshore during spring, summer and autumn [*Breaker and Mooers*, 1986; *Strub et al.*, 1991; *Rosenfeld et al.*, 1994; *Tseng and Ferziger*, 2001]. The NHY effects may enhance the growth of meanders and filaments of upwelled water [*Chao and Shaw*, 2002] from late spring to summer. Most filaments occur in summer, forming cold and warm mushroom-like patterns at multiple scales, especially south of Monterey Bay (see Figure 10 for an example). On a shorter timescale, the results are likely to show even larger NHY effects in summer. The horizontal and vertical velocity difference shows strong NHY effects in the area of Sur Ridge, which is an upwelling center during summer. In addition, the maximum magnitudes occur around 300 m where the CUC is the strongest (Figures 17–20). It appears that the NHY effects are important to the accurate representation of undercurrent transition across Monterey Canyon. It is clear that the interaction between CUC and near-surface CC (including upwelling filaments, eddies) results in strong vertical shear in the shallow region (Figure 12). We believe the CUC, near-surface CC and their interaction with local bathymetry play important roles to trigger the significant NHY effects in summer [*Tseng*, 2003]. However,

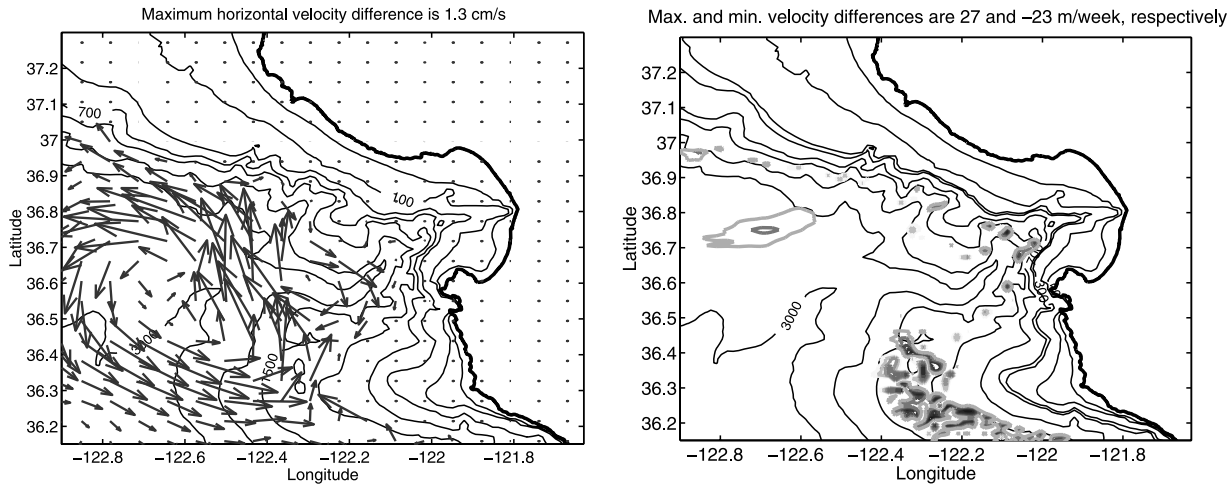

Figure 21. Velocity difference field between HY and NHY models at depth 1000 m using the high-resolution MBARM models. The velocity field is yearly averaged from year 6. (a) Horizontal velocity difference and (b) vertical velocity difference contours. See color version of this figure in the HTML.

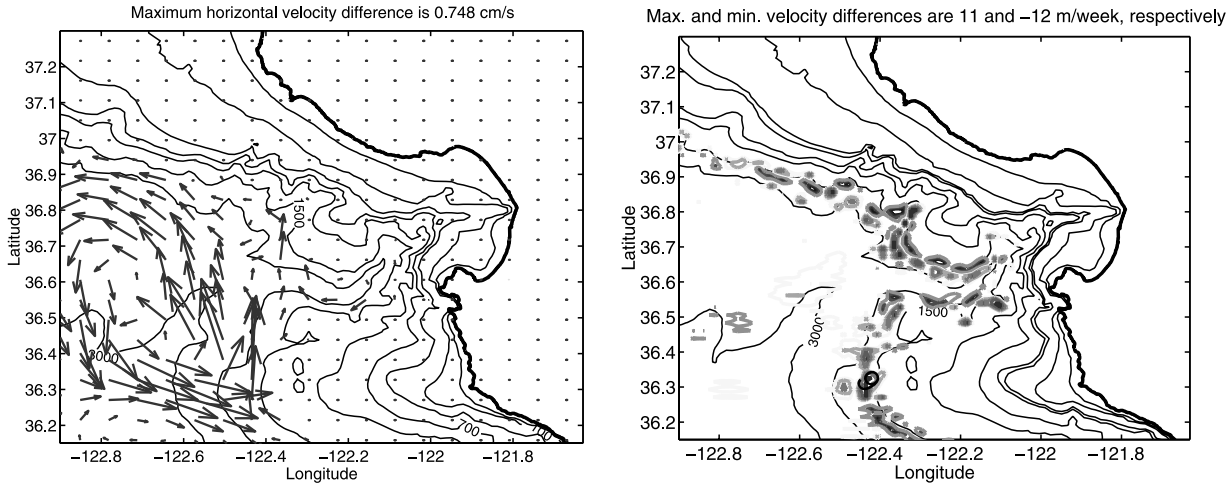

Figure 22. Velocity difference field between HY and NHY models at depth 1500 m using the high-resolution MBARM models. The velocity field is yearly averaged from year 6. (a) Horizontal velocity difference and (b) vertical velocity difference contours. See color version of this figure in the HTML.

the mechanism is still not clear and difficult to analyze since the lateral open boundary and seasonally varying flow complicate the analysis. The dynamics of the above three-way interaction requires further investigation using simplified bathymetry and a NHY model and is beyond the scope of this study.

[45] The difference between HY and NHY models is reduced after autumn. Note that the difference in winter is still significant in the shallow region but is small in the deep ocean (>1000 m). Surface-trapped NHY fronts may occur almost anywhere, because the radius of deformation of small-scale surface trapped modes is small. This NHY effect is more significant during winter when the near-surface stratification is weaker than during summer. Autumn is the season in which the dominant flow changes from equatorward to poleward in the upper ocean. By October, upwelling favorable circulation occurs much less frequently, and near-surface flow along the central coast is under the influence of the northward flowing Davidson Current, which generally reaches its maximum speed at the surface in December [*Paduan and Rosenfeld*, 1996].

[46] It is noteworthy that hydrostatically modeled systems actually have more total energy than the corresponding NHY systems. Specifically, the potential energy decrease due to sinking dense fluid and rising warm fluid goes entirely into horizontal kinetic energy according to the HY equations.

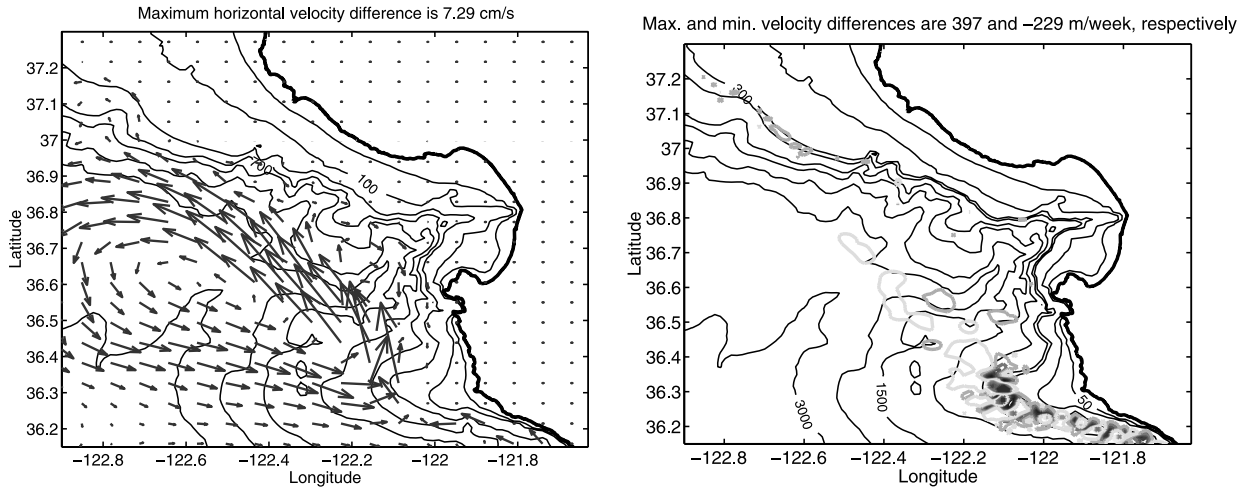

Figure 23. Velocity difference field between HY and NHY models at depth 300 m using the high-resolution MBARM models. The velocity field is yearly averaged from year 7. (a) Horizontal velocity difference and (b) vertical velocity difference contours. See color version of this figure in the HTML.

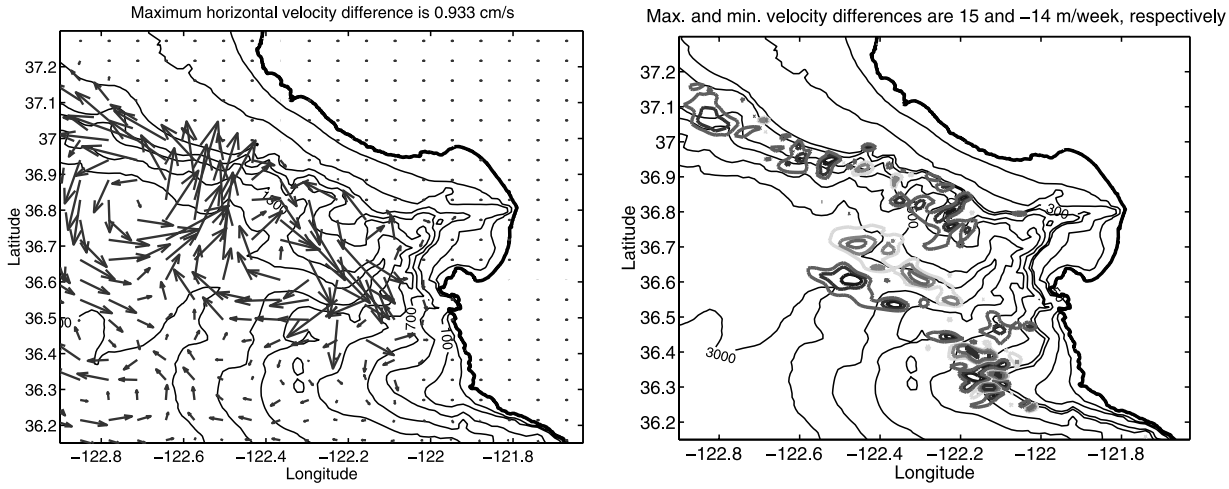

Figure 24. Averaged velocity differences between two consecutive years (years 6 and 7) at depth 300 m using the high-resolution, nonhydrostatic MBARM models. (a) Horizontal velocity difference and (b) vertical velocity difference contours. See color version of this figure in the HTML.

Vertical acceleration senses no inertia, generally leading to larger vertical acceleration than would occur when inertia terms are included in the vertical momentum equation. The HY approximation is well posed and robust in spite of its lack of energy conservation. The horizontal kinetic energy is limited by the potential energy release while the vertical kinetic energy is limited by its relation to horizontal velocity through the incompressibility equation.

5. Nonhydrostatic Factor

[47] The above section indicates that significant differences are found between the HY and NHY models. These differences are consistent with the differences between the data-assimilated HY model results and observation [*Paduan and Shulman*, 2004]. In order to further quantify NHY effects, we compare the NHY and HY diagnostic terms in the momentum equation of the NHY model. NHY effects are by definition due to the vertical acceleration terms. The NHY effects are small for features with large horizontal scales compared to the vertical. The hydrostatic "primitive equations" neglect these terms. The nonhydrostatic terms (NHT) include the local vertical acceleration ($\partial w/\partial t$) and the horizontal and vertical advection. We normalize the NHT by the RMS value of the buoyancy term $\langle \rho' g \rangle$, so that the nonhydrostatic factor (NHF) is

$$\mathrm{NHF} = \frac{\mathrm{NHT}}{\rho' g} = \frac{\langle \frac{\partial w}{\partial t} + u\frac{\partial w}{\partial x} + v\frac{\partial w}{\partial y} + w\frac{\partial w}{\partial z} \rangle}{\langle \rho' g \rangle} \tag{9}$$

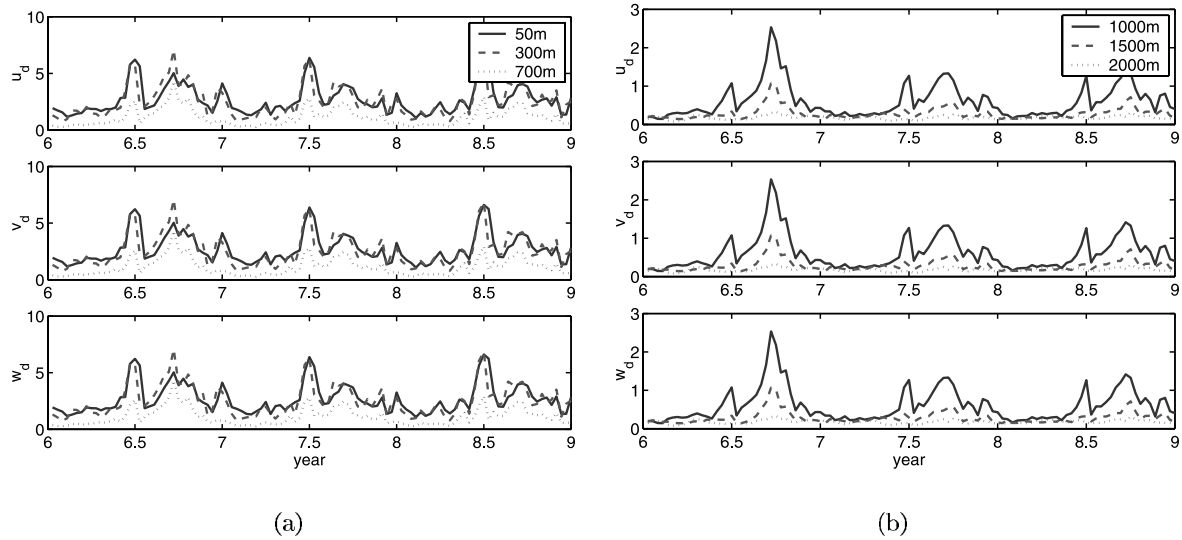

Figure 25. (a and b) Time series plane-averaged RMS velocity difference (cm/s) at various depths (u_d, RMS velocity difference in horizontal velocity u; v_d, RMS velocity difference in horizontal velocity v; w_d, RMS velocity difference in vertical velocity w) between HY and NHY models within year 6 to year 8. See color version of this figure in the HTML.

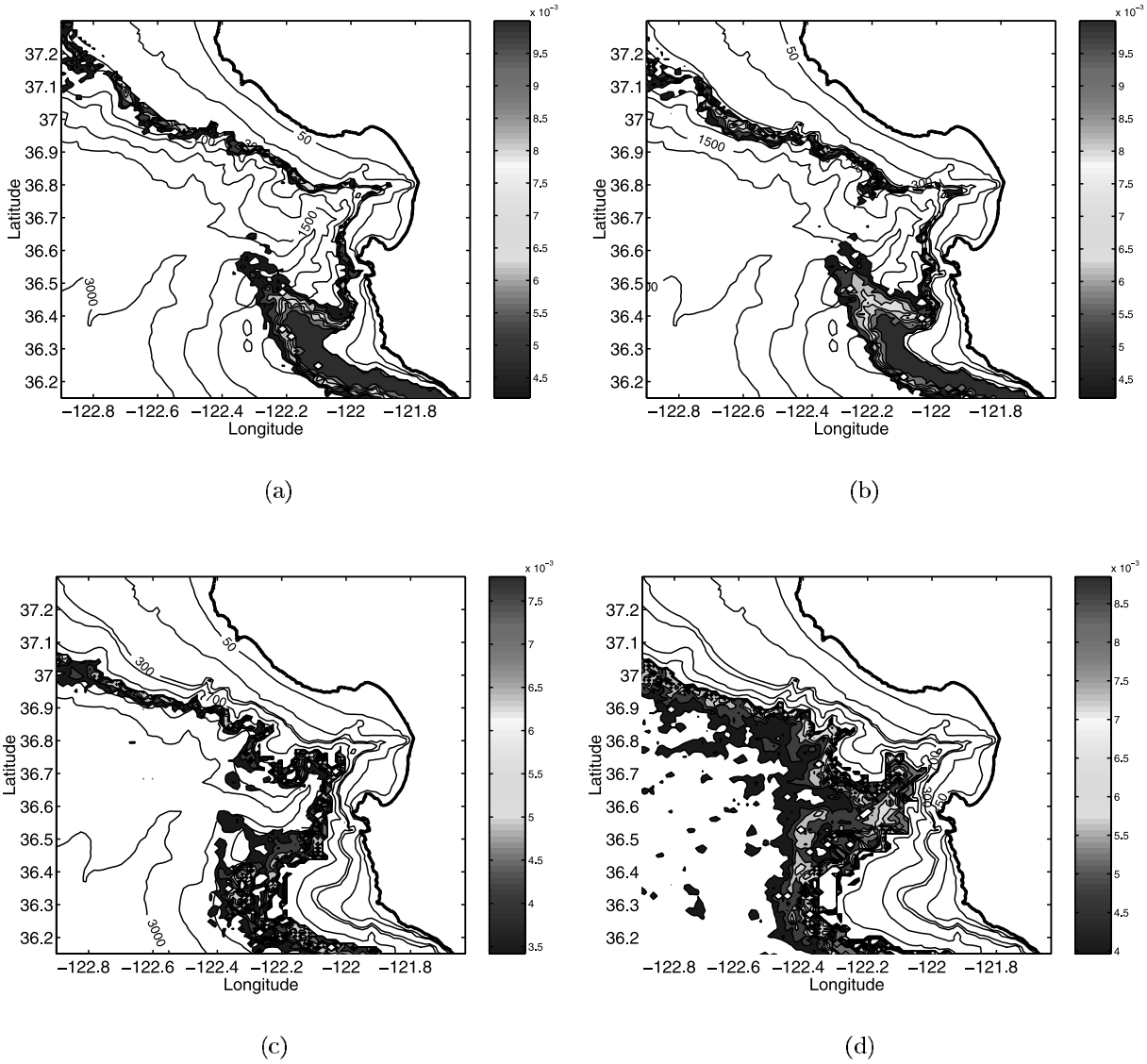

Figure 26. Annually averaged, normalized NHF at four different depths: (a) 250 m, (b) 360 m, (c) 880 m, and (d) 1150 m. Red color represents values that are greater than 1×10^{-2}. The maximum value is $O(10)$ locally. See color version of this figure in the HTML.

where $\rho' = (\rho - \overline{\rho})/\rho_0$; $\overline{\rho}$ is the horizontal mean density (varying with depth) and ρ_0 is the background density. The normalization factor ($\langle \rho' g \rangle$) measures the size of the hydrostatic terms. Removing the horizontal mean density has no effect on the hydrostatic flow so this is a good normalization.

[48] The yearly averaged, normalized NHF at various depths is shown in Figure 26 (250 m, 360 m, 880 m, 1150 m). The shading area indicates the region in which the NHF is in excess of 3.5×10^{-3}. The NHF is nearly zero in a large portion of the simulation domain, the exception being near sloping bathymetry, which is consistent with the results given above which showed that NHY effects are important in the canyon and in the nearshore region (particularly Sur Ridge). The HY approximation is appropriate elsewhere. The maximum normalized NHF is $O(10)$ but the red shading indicates the region in which the NHF is in excess of 1×10^{-2}. This suggests that NHY effects are very important in coastal ocean modeling. These results are consistent with previous discussion. In shallow region, NHY effects are important when strong CUC flows toward and across Sur Ridge. The steering effect of local topography enhances the deviation of vertical acceleration in HY approximation. At depth, nonhydrostatic effects are important inside the MSC because of its steep bathymetry. It is apparent that the local bathymetry plays an important role on forcing the vertical acceleration beyond hydrostatic expectation under some circumstances. It has also been shown by *Chao and Shaw* [2002] that the growth rate of instability could be affected by the NHY modes.

[49] The complex geometry increases the nonlinearity and alters the mesoscale coastal circulation. There are significant differences in the regional circulation patterns between HY and NHY models. The change in horizontal and vertical transport may significantly affect small-scale turbulent mixing near the coast. These complex and en-

hanced coastal transport processes cannot be correctly interpreted using HY models.

6. Summary

[50] The high-resolution MBARM was used to investigate the regional ocean circulation in the Monterey Bay area. The model is nonhydrostatic and has the immersed boundary module built into it. The model is tightly coupled to a large-scale CCS model and reproduces several known features of the regional circulation in the vicinity of Monterey Bay.

[51] We investigated the nonhydrostatic effects on regional circulation in this area. We showed that deep Monterey Canyon and Sur Ridge contribute significantly to the nonhydrostatic effects by comparing the HY and NHY model results. The hydrostatic model produces a false cyclonic eddy in the canyon, which is consistent with previous HY model [*Paduan and Shulman*, 2004]. The comparison illustrates that the hydrostatic approximation error influences the regional circulation in the vicinity of Monterey Bay and can be significantly reduced by using a NHY model. Most previous studies used idealized geometry and filtered bathymetry, which is too smooth to realistically represent Monterey Canyon. We conclude that the hydrostatic approximation may be inappropriate for dealing with the complex circulation in this area. In particular, nonhydrostatic effects play an important role in determining the nonlinear dynamics in summer circulation. The nonlinear, nonhydrostatic dynamics are enhanced by the complex coastal geometry and, in some circumstance, cannot be ignored in coastal ocean modeling.

[52] **Acknowledgments.** The authors thank Robert Haney for providing the CCS large-scale models. Many thanks are due to Robert Street and Leslie Rosenfeld for their useful discussions, Florence Wang and Steven Eittreim for providing the Monterey Bay topography, and MBARI and the RAD Laboratory at the Naval Postgraduate School for providing the observation data. Financial support for this work was provided by NASA Ames Center for Turbulent Research, Stanford, and partially by NSF ITR/AP (GEO) grant 0113111 (B. Fossum, Program Manager). Comments from Laurence Breaker and two anonymous reviewers are deeply appreciated.

References

Allen, S. E., M. S. Dinniman, J. M. Klinck, D. D. Gorby, A. J. Hewett, and B. M. Hickey (2003), On vertical advection truncation errors in terrain-following numerical models: Comparison to a laboratory model for upwelling over submarine canyons, *J. Geophys. Res.*, *108*(C1), 3003, doi:10.1029/2001JC000978.

Batteen, M. L. (1997), Wind-forced modeling studies of currents, meanders, and eddies in the California Current System, *J. Geophys. Res.*, *102*, 985–1010.

Batteen, M. L., and P. W. Vance (1998), Modeling studies of the effects of wind forcing and thermohaline gradients on the California Current System, *Deep Sea Res., Part II*, *45*, 1507–1556.

Blumberg, A. F., and G. L. Mellor (1987), A description of a three-dimensional coastal ocean circulation model, in *Three-Dimensional Coastal Ocean Models*, *Coastal Estuarine Sci.*, vol. 4, edited by N. S. Heaps, pp. 1–16.

Breaker, L. C., and W. W. Broenkow (1994), The circulation of Monterey Bay and related processes, *Oceanogr. Mar. Biol.*, *32*, 1–64.

Breaker, L. C., and C. N. K. Mooers (1986), Oceanic variability off the central California coast, *Progr. Oceanogr.*, *17*, 61–135.

Brink, K. H., and T. J. Cowles (1991), The Coastal Transition Zone Program, *J. Geophys. Res.*, *96*, 14,637–14,647.

Casulli, V., and G. S. Stelling (1998), Numerical simulation of 3D quasi-hydrostatic, free-surface flow, *J. Hydraul. Eng.*, *124*, 678–686.

Chao, S. Y., and P. T. Shaw (2002), Nonhydrostatic aspects of coastal upwelling meanders and filaments off eastern ocean boundaries, *Tellus, Ser. A*, *54*, 63–75.

Chao, Y., Z. Li, P. Marchesiello, J. C. McWilliams, and F. Chavez (2002), Modeling the mean circulation and seasonal cycle of Monterey Bay, California, *Eos Trans. AGU*, *83*, Ocean Sci. Meet. Suppl., Abstract OS11O-08.

Chelton, D. B. (1984), Seasonal variability of alongshore geostrophic velocity off central California, *J. Geophys. Res.*, *89*, 3473–3486.

Collins, C. A., N. Garfield, T. A. Rago, F. W. Rischmiller, and E. Carter (2000), Mean structure of the inshore countercurrent and California Undercurrent off Point Sur, California, *Deep Sea Res., Part II*, *47*, 765–782.

Dietrich, D. E. (1997), Application of a modified "a" grid ocean model having reduced numerical dispersion to the Gulf of Mexico circulation, *Dyn. Atmos. Oceans*, *27*, 201–217.

Dietrich, D. E., and C. A. Lin (2002), Effects of hydrostatic approximation and resolution on the simulation of convective adjustment, *Tellus, Ser. A*, *54*, 34–43.

Dietrich, D. E., M. G. Marietta, and P. J. Roache (1987), An ocean modeling system with turbulent boundary layers and topography: Part 1. Numerical studies of small island wakes in the ocean, *Int. J. Numer. Methods Fluids*, *7*, 833–855.

Dietrich, D. E., A. Mehra, R. L. Haney, M. J. Bowman, and Y. H. Tseng (2004a), Dissipation effects in North Atlantic Ocean modeling, *Geophys. Res. Lett.*, *31*, L05302, doi:10.1029/2003GL019015.

Dietrich, D. E., R. L. Haney, V. Fernandez, S. Josey, and J. Tintore (2004b), Air-sea fluxes based on observed annual cycle surfce climatology and ocean model internal dynamics: A precise, non-damping zero-phase-lag approach applied to the Mediterranean Sea, *J. Mar. Syst.*, *52*, 145–165.

Dukowicz, J. K., R. D. Smith, and R. C. Malone (1993), A reformulation and implementation of the Bryan-Cox-Semtner ocean model on the connection machine, *J. Atmos. Oceanic Technol.*, *10*, 195–208.

Ferziger, J. H., and Y. H. Tseng (2004), A coordinate system independent streamwise upwind method for fluid flow computation, *Int. J. Numer. Methods Fluids*, *45*, 1235–1247.

Haney, R. L. (1991), On the pressure gradient force over steep topography in sigma coordinate ocean models, *J. Phys. Oceanogr.*, *21*, 610–619.

Haney, R. L., R. A. Hale, and D. E. Dietrich (2001), Offshore propagation of eddy kinetic energy in the California Current, *J. Geophys. Res.*, *106*, 11,709–11,717.

Hellerman, S., and M. Rosenstein (1983), Normal monthly wind stress over the world ocean with error estimates, *J. Phys. Oceanogr.*, *13*, 1093–1104.

Hickey, B. M. (1979), The California Current System: Hypotheses and facts, *Progr. Oceanogr.*, *8*, 191–279.

Legg, S., and A. Adcroft (2003), Internal wave breaking at concave and convex continental slopes, *J. Phys. Oceanogr.*, *33*, 2224–2246.

Levitus, S. (1982), Climatological atlas of the world oceans, *NOAA Prof. Pap. 13*, 173 pp., U.S. Govt. Print. Off., Washington, D. C.

Lewis, J. K., I. Shulman, and F. Blumberg (1998), Assimilation of Doppler radar current data into numerical ocean models, *Cont. Shelf Res.*, *18*, 541–559.

Lu, Y. Y., D. G. Wright, and D. Brickman (2001), Internal tide generation over topography: Experiments with a free-surface *z*-level ocean model, *J. Atmos. Oceanic Technol.*, *18*, 1076–1091.

Ly, L. N., and P. A. Luong (1999), Numerical grid used in a coastal ocean model with breaking wave effects, *J. Comput. Appl. Math*, *103*, 125–137.

Lynn, R. J., and J. J. Simpson (1987), The California Current System: The seasonal variability of its physical characteristics, *J. Geophys. Res.*, *92*, 12,947–12,966.

Mahadevan, A., J. Oliger, and R. Street (1996), A nonhydrostatic mesoscale ocean model. Part I: Well-posedness and scaling, *J. Phys. Oceanogr.*, *26*, 1868–1880.

Marchesiello, P., J. C. McWilliams, and A. Shchepetkin (2003), Equilibrium structure and dynamics of the California Current System, *J. Phys. Oceanogr.*, *32*, 753–783.

Mooers, C. N. K., and A. R. Robinson (1984), Turbulent jets and eddies in the California Current and inferred cross-shore transport, *Science*, *223*, 51–53.

Mooers, C. N. K., C. A. Collins, and R. L. Smith (1976), Dynamic structure of frontal zone in coastal upwelling region off Oregon, *J. Phys. Oceanogr.*, *6*, 3–21.

Narimousa, S., and T. Maxworthy (1989), Application of a laboratory model to the interpretation of satellite and field observations of coastal upwelling, *Dyn. Atmos. Oceans*, *13*, 1–46.

Narimousa, S., and T. Maxworthy (1991), Experiments on the structure and dynamics of forced, quasi-two-dimensional turbulence, *J. Fluid Mech.*, *223*, 113–133.

Oliger, J., and A. Sundstrom (1978), Theoretical and practical aspects of some initial boundary value problems in fluid dynamics, *SIAM J. Appl. Math.*, *35*, 419–446.

Orlanski, I. (1976), A simple boundary condition for unbounded hyperbolic flows, *J. Comput. Phys.*, *21*, 251–269.

Pacanowski, R. C., and S. G. H. Philander (1981), Parameterization of vertical mixing in numerical models of tropical ocean, *J. Phys. Oceanogr.*, *11*, 1443–1451.

Paduan, J. D., and L. K. Rosenfeld (1996), Remotely sensed surface currents in Monterey Bay from shore-based HF radar (Coastal Ocean Dynamics Application Radar), *J. Geophys. Res.*, *101*, 20,669–20,686.

Paduan, J. D., and I. Shulman (2004), HF radar data assimilation in the Monterey Bay area, *J. Geophys. Res.*, *109*, C07S09, doi:10.1029/2003JC001949.

Palma, E. D., and R. P. Matano (2000), On the implementation of open boundary condition for a general circulation model: The three-dimensional case, *J. Geophys. Res.*, *105*, 8605–8627.

Petruncio, E. T., J. D. Paduan, and L. K. Rosenfeld (2002), Numerical simulations of the internal tide in a submarine canyon, *Ocean Modell. 4*, pp. 221–249, Hooke Inst. Oxford Univ., Oxford, U. K.

Pierce, S. D., R. L. Smith, P. M. Kosro, J. A. Barth, and C. D. Wilson (2000), Continuity of the poleward undercurrent along the eastern boundary of the mid-latitude Pacific, *Deep Sea Res., Part II*, *47*, 811–829.

Ramp, S. R., L. K. Rosenfeld, T. D. Tisch, and M. R. Hicks (1997), Moored observations of the current and temperature structure over the continental slop off central California: 1. A basic description of the variability, *J. Geophys. Res.*, *102*, 22,877–22,902.

Roache, P. J. (1995), *Elliptic Marching Methods and Domain Decomposition*, CRC Press, Boca Raton, Fla.

Rosenfeld, L. K., F. B. Schwing, N. Garfield, and D. E. Tracy (1994), Bifurcated flow from an upwelling center: A cold water source for Monterey Bay, *Cont. Shelf Res.*, *14*, 931–964.

Rosenfeld, L. K., T. Anderson, G. Hatcher, J. Roughgarden, and Y. Shkedy (1995), Upwelling fronts and barnacle recruitment in central California, *MBARI Tech. Rep. 95-19*, Monterey Bay Acquarium Res. Inst., Moss Landing, Calif.

Rosenfeld, L. K., J. D. Paduan, E. T. Petruncio, and J. E. Gocalves (1999), Numerical simulations and observations of the internal tide in a submarine canyon, paper presented at 11th 'Aha Huliko'a Hawaiian Winter Workshop, Dep. of Oceanogr., Sch. of Ocean and Earth Sci. and Technol., Univ. of Hawaii, Honolulu, 19–22 Jan.

Sanderson, B. G. (1998), Order and resolution for computational ocean dynamics, *J. Phys. Oceanogr.*, *28*, 1271–1286.

Sanderson, B. G., and G. Brassington (1998), Accuracy in the context of a control-volume model, *Atmos. Ocean*, *36*, 355–384.

Shulman, I., C. R. Wu, J. K. Lewis, J. D. Paduan, L. K. Rosenfeld, J. C. Kindle, S. R. Ramp, and C. A. Collins (2002), High resolution modeling and data assimilation in the Monterey Bay area, *Cont. Shelf Res.*, *22*, 1129–1151.

Smith, R. D., J. K. Dukowicz, and R. C. Malone (1992), Parallel ocean general circulation modeling, *Physica D*, *60*, 38–61.

Staneva, J. V., D. E. Dietrich, E. V. Stanev, and M. J. Bowman (2001), Rim current and coastal eddy mechanisms in an eddy-resolving Black Sea general circulation model, *J. Mar. Syst.*, *31*, 137–157.

Strub, P. T., P. M. Kosro, and A. Huyer (1991), The nature of the cold filaments in the California Current System, *J. Geophys. Res.*, *96*, 14,743–14,768.

Tadepalli, S. (1997), Numerical simulation and prediction of upwelling flow, Ph.D. thesis, Stanford Univ., Stanford, Calif.

Traganza, E. D., D. A. Nestor, and A. K. McDonald (1980), Satellite observations of a nutrient upwelling off the coast of California, *J. Geophys. Res.*, *85*, 4101–4106.

Tseng, Y. H. (2003), On the development of a ghost-cell immersed boundary method and its application to large eddy simulation and geophysical fluid dynamics, Ph.D. thesis, Stanford Univ., Stanford, Calif.

Tseng, Y. H., and D. E. Dietrich (2005), Entrainment and transport in idealized three-dimensional gravity current simulation, *J. Atmos. Oceanic Technol.*, in press.

Tseng, Y. H., and J. H. Ferziger (2001), Effects of coastal geometry and the formation of cyclonic/anti-cyclonic eddies on turbulent mixing in upwelling simulation, *J. Turbulence*, *2*, 014.

Tseng, Y. H., and J. H. Ferziger (2003), A ghost-cell immersed boundary method for flow in complex geometry, *J. Comput. Phys.*, *192*, 593–623.

Tseng, Y. H., and J. H. Ferziger (2004), Large-eddy simulation of turbulent wavy boundary flow: Illustration of vortex dynamics, *J. Turbulence*, *5*, 34.

Wong, F. L., and S. E. Eittreim (2001), Continental shelf GIS for the Monterey Bay National Marine Sanctuary, *U.S. Geol. Surv. Open File Rep.*, *01-179*.

D. E. Dietrich, AcuSea Inc., 1421 Monte Largo, Albuquerque, NM 87112, USA.

J. H. Ferziger, Environmental Fluid Mechanics Laboratory, Stanford University, Stanford, CA 94305-4020, USA.

Y.-H. Tseng, Computational Research Division, Lawrence Berkeley National Laboratory, 1 Cyclotron Road, Berkeley, CA 94720-1650, USA. (yhtseng@lbl.gov)